Title
Spin-Orbit Torques in Ferrimagnets and Topological Insulators

Author
Roschewsky, Niklas

Publication Date
2019

Peer reviewed|Thesis/dissertation

Spin-Orbit Torques in Ferrimagnets and Topological Insulators

by

Niklas Roschewsky

A dissertation submitted in partial satisfaction of the

requirements for the degree of

Doctor of Philosophy

in

Physics

in the

Graduate Division

of the

University of California, Berkeley

Committee in charge:

Professor Sayeef Salahuddin, Co-chair
Professor Frances Hellman, Co-chair
Professor Ronald Gronsky
Professor Zi Qiu

Spring 2019

Spin-Orbit Torques in Ferrimagnets and Topological Insulators

Abstract

Spin-Orbit Torques in Ferrimagnets and Topological Insulators

by

Niklas Roschewsky

Doctor of Philosophy in Physics

University of California, Berkeley

Professor Sayeef Salahuddin, Co-chair

Professor Frances Hellman, Co-chair

In the field of spintronics, the transport of spin and charge is explored. Within the last decade, significant progress has been made towards the understanding of spin-charge coupling in metallic systems. Further, novel spintronic device applications have been realized. In this regard, spin-orbit torque is of particular interest, as it enables the manipulation of magnetic ordering and has been proven to be useful for memory and logic applications. Here, spin-orbit torque describes the generation of a pure spin current via the spin-Hall effect in a heavy metal or the Rashba-Edelstein effect in a heavy metal/ferromagnet interface. When the spin-current diffuses into an adjacent ferromagnet, the magnet generally experiences a torque and thus magnetization dynamics is excited.

In this thesis, we investigate spin-orbit torque in transition metal-rare earth ferrimagnets. While these ferrimagnets provide technological advantages compared to ferromagnets, such as magnetization tunability and bulk perpendicular magnetic anisotropy, the angular momentum transfer process has not been well understood. We show that the spin-orbit torque driven angular momentum transfer follows the sign of the total magnetization, while transport-based effects such as the anomalous Hall effect are only sensitive to the transition metal magnetization. Further, we demonstrate the spin-orbit torque switching of ultra-thick GdFeCo films and show that GdFeCo is a promising material for magnetic memory devices due to a high spin-orbit torque switching efficiency j_c/Δ.

In the second part of this thesis, we study spin-orbit torques in topological insulator/ ferromagnet heterostructures. To this end, harmonic Hall measurements are performed in BiSb/Co heterostructures. We find a large second harmonic voltage response stemming from the ordinary Nernst effect, while signatures of spin-orbit torque are absent. This is in contrast to a recent report in literature reporting spin-Hall angles significantly larger than unity. We conclude that the ordinary Nernst effect can be a spurious signal in harmonic Hall measurements where the in-plane magnetic field is rotated in the film plane.

The third part of this thesis discusses the influence of mechanical stress on the performance of magnetic tunnel junctions for spin-transfer torque magnetic random access memory. To this end, a 4-point bending setup that allows the application of constant stress over a large substrate area is developed. We find that the performance of the magnetic tunnel junctions is very robust to external stress with changes in tunnel magneto-resistance (TMR), switching current I_c, and thermal stability Δ less than 2 %.

Für meine Eltern, Dörthe and Frank

Contents

Contents **ii**

1 The Role of Magnetism for Non-Voltatile Memory **1**

2 Theory of Spin Torque **5**
2.1 Spin-Orbit Coupling 5
2.2 Rashba-Edelstein Effect 6
2.3 Spin-Hall Effect 7
2.4 Spin-Orbit Torque 8

3 Electric Transport Characerization of Spin Torque **11**
3.1 Harmonic Measurements of Spin-Orbit Torque 12
3.2 Current Induced Magnetization switching 18
3.3 Thermal Stability Characterization 19

4 Spin-Orbit Torque in RE-TM Ferrimagnets **21**
4.1 The Role of the Magnetic Sublattice 21
4.2 Magnetic coupling in ferrimagnetic GdFeCo 21
4.3 Sample growth and fabrication 22
4.4 The anomalous Hall effect 23
4.5 Spin-orbit torque switching 25
4.6 Harmonic Hall measuremets of spin-orbit torque 25
4.7 Angular momentum transfer in TM/RE magnets 27

5 Thickness scaling of Spin-Orbit Torque **29**
5.1 Bulk Magnetic Anisotropy and Thickness Scaling 29
5.2 Sputter Deposition of GdFeCo 31
5.3 Spin-Orbit Torque Induces Effective Fields 31
5.4 Switching Phase Diagram in GdFeCo 36
5.5 Measurements of the Thermal Stability 36
5.6 Spin-Torques at Different Gd Concentration 37
5.7 Efficient SOT switching in GdFeCo 37

6 Spin-Orbit Torque in Topological Insulators **39**
6.1 Spin Current Generation at Topological Insulators Interfaces 39
6.2 The Ordinary Nernst Effect in Topological Insulators 40
6.3 Epitaxial growth of Bi-Sb 41
6.4 Harmonic Hall Measurements of Thermal Effects in Bi-Sb 42
6.5 Angular Dependence of the Harmonic Voltage 43
6.6 Magnetic Field Scaling of the Ordinary Nernst Effect in Bi-Sb 44
6.7 Power Scaling of the Ordinary Nerst Effect 46
6.8 Summary and Conclusions 46

7 MRAM Performance Under Mechanical Strain **48**
7.1 Strain in MTJ with Perpendicular Magnetic Anisotropy 48
7.2 4-point Bending Setup for Application of Constant Strain 49
7.3 Stress Dependence of the Tunnel Magneto Resistance 50
7.4 Spin Torque Switching 50
7.5 Thermal Stability Characterization 52
7.6 Robust MTJ Performance under Strain 53

8 Conclusions and Outlook **55**

Bibliography **59**

Acknowledgments

First and foremost, I thank my advisor Sayeef Salahuddin for welcoming me into his research group and for supporting my research for the past 4 years. I am especially grateful for the intellectual freedom and trust that he gave me during my PhD studies. Furthermore, I would like to thank my co-advisor Frances Hellman for many fruitful discussions and indispensable advice. In addition, I thank my PhD committee members Zi Qui, Ronald Gronsky, and Joel Moore.

The work in this thesis is a product of fruitful collaborations during the last four years. Special thanks goes to Emily Walker and Seth Bank for providing the bithmuth antimonide samples; as well as Tomoya Matsumura, Takeshi Kato, and Charles-Henri Lambert for providing the GdFeCo samples that were characterized in this thesis.

During the summer of 2017, I had the chance to do an internship in the New Memory Technology group at Samsung Semiconductor Inc. in San Jose. I learned a lot, far beyond spin-transfer torque memory, thanks to the help of a great team and a perfect work environment. My special thanks goes to Vladimir Nikitin and Sebastian Schafer, who were always available to answer my questions and assisted me in the laboratory countless times. In addition, I thank Robert Beach and Volodymy Voznyuk, not only for many scientific discussions but also for getting me back into rock climbing.

Next, I would like to thank all current and former members of the Salahuddin research group with whom I collaborated over the years (and who would join our lunches at the Curry House). My special thanks goes to Saidur Bakaul, Debanjan Bhowmik, Korok Chatterjee, Suraj Cheema, James Clarkson, Leonard Deuschle, Praveen Gowtham, Jason Hsu, Dominic Labanowski, Ahad Rauf, Shehrin Sayed, Samuel Smith, and Elizaveta Tremsina.

Finally, I would like to thank my friends and family. Whenever I went overboard during my PhD, Johannes would help me get back into the boat. Even when time was flying for Christian, we would find time to climb Indian Rock on Saturday nights. Without the help from my parents Dörthe and Frank, none of this work would have been possible. I am grateful for their help throughout every step of my life. Graduate school would not have been the same for me without Elizabeth, who is so much more than my life partner. Thank you for all the fish!

Chapter 1

The Role of Magnetism for Non-Voltatile Memory

Since the introduction of the first mass-produced computer, the *IBM 650* in 1953, digital memory has relied on magnetism. Read and write operations of early memory technologies, such as drum memory or core memory, were based on magnetic induction for read and write operations. The scaling of these memory technologies was limited by large ohmic losses associated with the high current densities necessary to generate sufficiently large magnetic fields for read and write operations. A breakthrough in the scaling of magnetic memory was seen with the discovery of the Giant Magnetoresistance (GMR) by Grünberg and Fert [33, 7], as well as the discovery of Tunnel Magnetoresistance (TMR) [50, 81]. Grünberg and Fert discovered that the resistance of a ferromagnet/normal metal/ferromagnet trilayer structure depends on the relative alignment of the two ferromagnetic layers (GMR). Similarly, the resistance of a ferromagnet/insulator/ferromagnet trilayer can change by more than 100 % if the relative alignment of the two ferromagnetic layers is changed from parallel to anti-parallel (TMR). The ferromagnet/insulator/ferromagnet trilayer structure is an important building block of modern memory technology and is referred to as magnetic tunnel junction (MTJ).

Modern hard disc drives (HDD) rely on the TMR effect for data readout. To this end, an MTJ is scanned in close proximity over a magnetic disc. The stray field from a small region of the magnetic disc is sufficient to reorient one of the ferromagnetic layers in the MTJ. The associated change in the resistance of the MTJ is used for the data readout. While high storage densities have been achieved in HDD, some disadvantages of this memory technology include intrinsically slow read and write speeds, large size of HDD, and sensitivity to mechanical motion. A modern memory approach is to use individual MTJs to store bits of information. While this approach is still non-volatile, higher read and write speeds can be archived, the bit size is reduced and no mechanical motion is necessary for data transfer. Therefore this technology is well suited as magnetic random access memory (MRAM).

The first commercial MRAM was introduced in 2006 and is based on toggle switching [27] of the ferromagnet in the MTJ. Here, one layer in the MTJ stack is switched by applying a magnetic field sequence. The magnetic field is generated via induction with the help of

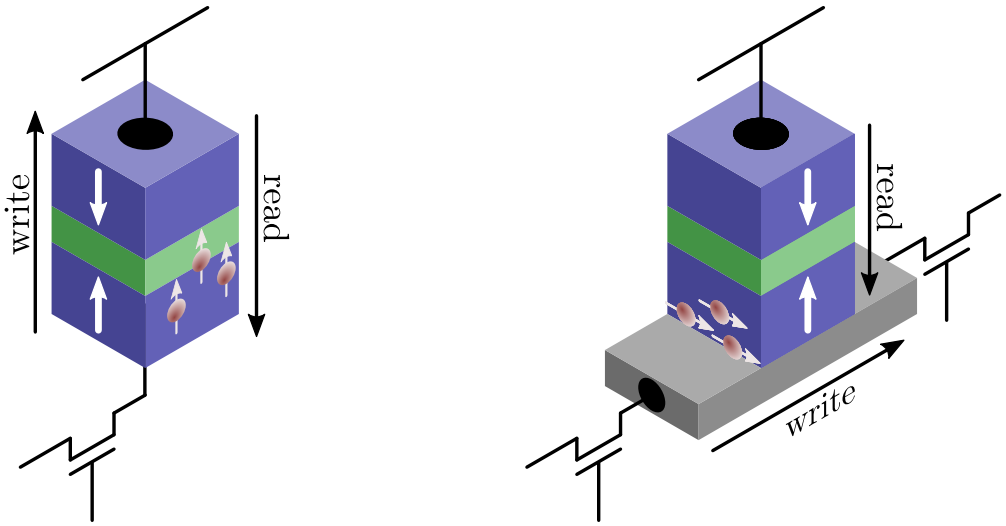

Figure 1.1: The left shows a two-terminal MRAM device. For the write operation, spin-transfer torque switching is used, while the state of the tunnel junction can be sensed with the tunnel magneto-resistance. The left shows a three-terminal MRAM device. Here, read and write paths are separated. While the tunnel magneto-resistance is still used for the read operation, spin-orbit torque is used for writing.

copper lines. Toggle MRAM has virtually infinite endurance, very fast write speeds, and high reliability. However, it is not scalable due to the need for large currents to generate magnetic fields. To overcome this issue, spin-transfer torque (STT), proposed by Slonczewski and Berger in 1996 [103, 11], can be used as an alternative switching mechanism. A spin-polarized current is used to switch the free layer of a MTJ. The spin-polarized current is generated by tunneling from a ferromagnet through an insulator. Since the switching mechanism is based on STT, this memory technology is referred to as STT-MRAM. STT-MRAM requires significantly less energy for the write process than toggle MRAM.

Recently, several manufactures announced the availability of embedded STT-MRAM modules for production in foundries [51, 102, 105]. While embedded STT-MRAM is significantly cheaper than embedded flash memory, a few key challenges remain to be solved for STT-MRAM. High current densities necessary for STT-switching can degrade MTJ tunnel barriers and cause low endurance. Further, a tunnel junction can be accidentally switched during the read process, since the read and write paths are the same. This process is called read-disturb [2]. Ideal MRAM memory would combine spin torque switching as found in STT-MRAM and separated read and write mechanisms, similar to toggle MRAM. This design is realized in spin-orbit torque MRAM [61], where a pure spin current is generated in a material with high spin-orbit coupling and injected into an adjacent ferromagnet. Spin-orbit torque switching was first demonstrated in 2012 by Miron et al. and Liu et al [79, 67]. They suggested that the spin current is generated via the Rashba-Edelstein effect or the spin Hall effect respectively.

Since the read and write paths in SOT-MRAM are separated, the endurance and read-disturb issues of STT-MRAM are solved. However, the reported switching efficiency in SOT-MRAM is lower compared to STT-MRAM. Here switching efficiency refers to the thermal stability factor Δ divided by the current needed to switch the magnet. In this thesis, we explore three approaches to increase the switching efficiency of SOT magnetic memory devices. First, the use of ferrimagnets (as opposed to ferromagnets) as a potential new material class for magnetic memory devices will be discussed. Afterwards, we evaluate the use of topological insulators as spin current generators for magnetic memory. Finally, we investigate the influence of mechanical strain on the memory performance of magnetic tunnel junctions. This thesis has been divided into eight chapters:

Chapter 1 An introduction to the field of spintronics, focusing on magnetic memory applications. We outline the content of this thesis.

Chapter 2 A brief summary of the theory of spin-orbit coupling and spin-orbit torque is given. The purpose of this chapter is to give a short theoretical background necessary for the understanding of the following chapters.

Chapter 3 In the main part of this thesis, spin-orbit torque experiments are analyzed and discussed. This chapter serves as an introduction to the experimental methods used in this thesis. In particular, we discuss experimental setups for harmonic Hall measurements, spin-orbit torque switching, and thermal stability characterization.

Chapter 4 Spin-orbit torque in ferrimagnetic GdFeCo is discussed. GdFeCo is a rare earth-transition metal magnet. We find that the angular momentum transfer is proportional to the total magnetization, while transport-based effects such as the anomalous Hall effect are only sensitive to the transition metal magnetization. The results are published in [96].

Chapter 5 This chapter discusses the thickness scaling of spin-orbit torque. A discussion of the spin-torque dependence on the thickness of the magnetic layer has been elusive in literature so far due to the lack of suitable materials with perpendicular magnetic anisotropy. Here, we show that ultra-thick GdFeCo has a high switching efficiency and may be well-suited for memory applications. The results are published in [95].

Chapter 6 Harmonic Hall voltage measurements in topological insulator/ferromagnet heterostructures are discussed. While signatures of spin-orbit torque are absent in our measurements, large thermal voltages stemming from the ordinary Nernst effect are observed. This is in contrast to recent reports in literature, where large spin- to charge current conversion efficiencies are observed. The results are published in [94].

Chapter 7 In this chapter, we investigate the performance of magnetic tunnel junctions for MRAM applications under the influence of mechanical stress. We find that important performance parameters such as the tunnel magneto-resistance, the critical current, or

the thermal stability are very robust to external strain with changes less than 2 % over the entire measurement range. This work is the result of an internship in the New Memory Technology group at Samsung Semiconductor Inc. The results are published in [93].

Chapter 8 This chapter summarizes the thesis and includes an outlook with open questions and future projects.

Publications

The results reported in this thesis have been published in different journals. This is an overview of these publications:

Niklas Roschewsky et al. "Perpendicular magnetic tunnel junction performance under mechanical strain". In: *Applied Physics Letters* 112.23 (June 2018), p. 232401. ISSN: 0003-6951. DOI: 10.1063/1.5034145. URL: http://aip.scitation.org/doi/10.1063/1.5034145.

Niklas Roschewsky et al. "Spin-orbit torque and Nernst effect in Bi-Sb/Co heterostructures". In: *Physical Review B* 99.19 (May 2019), p. 195103. ISSN: 2469-9950. DOI: 10.1103/PhysRevB.99.195103. URL: https://link.aps.org/doi/10.1103/PhysRevB.99.195103.

Niklas Roschewsky et al. "Spin-orbit torque switching of ultralarge-thickness ferrimagnetic GdFeCo". In: *Physical Review B* 96.6 (Aug. 2017), p. 064406. ISSN: 2469-9950. DOI: 10.1103/PhysRevB.96.064406. URL: http://link.aps.org/doi/10.1103/PhysRevB.96.064406.

Niklas Roschewsky et al. "Spin-orbit torques in ferrimagnetic GdFeCo alloys". In: *Appl. Phys. Lett.* 109 (2016), p. 112403. DOI: 10.1063/1.4962812.

Chapter 2

Theory of Spin Torque

2.1 Spin-Orbit Coupling

The magnetic moment of an electron $\boldsymbol{\mu}$ is often considered a fundamental building block of a magnet. In atoms, $\boldsymbol{\mu}$ is proportional to the angular momentum $\boldsymbol{L}$ of the electron. The proportionality constant γ_e is called the gyromagnetic ratio:

$$\boldsymbol{\mu} = \gamma_e \boldsymbol{L} \ . \tag{2.1}$$

We will estimate γ_e by calculating the magnetic moment of an electron in a circular orbit of radius r around the nucleus. The electron carries a current $I = -e/\tau$. This circular current is associated with a magnetic moment $|\boldsymbol{\mu}| = I \cdot \pi r^2 = -e/\tau \cdot \pi r^2$. In addition, the electron carries angular momentum $|\boldsymbol{L}| = mvr = mr \cdot 2\pi r/\tau$. Using the expressions for $\boldsymbol{L}$ and $\boldsymbol{\mu}$ to eliminate τ we find:

$$\boldsymbol{\mu} = \underbrace{-\frac{e}{2m}}_{\gamma_e} \boldsymbol{L} \tag{2.2}$$

The negative sign indicates that the angular momentum of the electron is anti-parallel to the magnetic moment. The orbital angular momentum of the electron depends on the electronic configuration of the atom, described by the quantum numbers l and m_l. The Bohr magneton is defined as

$$\mu_B = \frac{e\hbar}{2m} = 9.274 \times 10^{-24}\,\mathrm{A\,m^{-1}}$$

so that the magnetic moment along the z axis can be written as $-m_l\mu_B$. The magnitude of the total magnetic dipole moment is $\sqrt{l(l+1)}\mu_B$.

Electrons are fermions with spin $s = 1/2$ and $m_s = \pm\hbar/2$. Thus, in addition to orbital angular momentum, the electron carries spin angular momentum. The magnitude of the spin angular momentum of the electron is $\sqrt{s(s+1)}\hbar = \sqrt{3}/2\hbar$. The value of the magnetic

moment along the quantization axis associated with the spin angular momentum is $\mu_s = -g\mu_B m_s$ and the magnitude is $\sqrt{3}/2g\mu_B$. Here, $g = 2.0023..$ is the magnetomechanical ratio or g-factor [42]. Thus, the spin magnetic moment of the electron is approximately $\mu_s \approx -\mu_B$.

The spin and orbital angular momentum of the electron combine to the total angular momentum $J = L+S$. If relativistic effects are considered, spin and orbital angular momentum couple and thus L and S are not conserved independently. The spin-orbit interactions is written as

$$H_{\mathrm{SO}} = \frac{e\hbar^2}{2m_e c^2 r}\frac{\mathrm{d}V(r)}{\mathrm{d}r}\boldsymbol{S}\cdot\boldsymbol{L}\ , \tag{2.3}$$

where c is the speed of light. Assuming an electron in a hydrogen-like Coulomb potential $V(r)$ with quantum numbers n and l, the spin-orbit coupling interaction energy is:

$$\langle H_{\mathrm{SO}}\rangle = \frac{Z^4 e^2\hbar^2}{4\pi\epsilon_0 a_0^3 n^3 l(l+1/2)(l+1)}\langle\boldsymbol{S}\cdot\boldsymbol{L}\rangle \tag{2.4}$$

Here, ϵ_0 is the vacuum permittivity and Z the atomic number. The Z^4 dependence indicates that spin-orbit coupling becomes significantly more important for heavy atoms. However, it should be noted that Z^4-dependence only holds for light atoms since the perturbation treatment breaks down at large atomic numbers. In solids, the spin-orbit coupling depends further on the band structure [42].

Spin-orbit coupling is important for the understanding of many physical phenomena. This includes mangeto-crystalline anisotropy, anisotropic mangneto-resistance, magnetic damping and anomalous Hall effect. For the theory of spin-orbit torque, the Rashba-Edelstein effect as well as the spin-Hall effect are of particular interest.

2.2 Rashba-Edelstein Effect

At the surface of a crystal, atomic periodicity is naturally broken. The uncompensated bonds can give rise to an electric field in the out of plane direction $\hat{\boldsymbol{z}}$. Electrons traveling with momentum $\boldsymbol{p}$ at the interface will experience a magnetic field perpendicular to the electric field and the direction of travel due to relativistic effects. This magnetic field couples to the electron spin and gives rise to the Rashba-Edelstein effect. The Rashba-Edelstein Hamiltonian can be written as:

$$H_{\mathrm{RE}} = \alpha_{\mathrm{R}}(\boldsymbol{\sigma}\times\boldsymbol{p})\cdot\hat{\boldsymbol{z}}\ .$$

Here $\alpha_{\mathrm{R}} = \gamma\mu_{\mathrm{B}}E_0/2mc^2$ is the Rashba constant and $\boldsymbol{\sigma}$ is the Pauli-matrix vector. H_{RE} couples momentum and spin direction of the electron and can give rise to a non-equilibrium spin-accumulation at the interface of a crystal. This is represented in Fig. 2.1 for the case of a spherical Fermi surface.

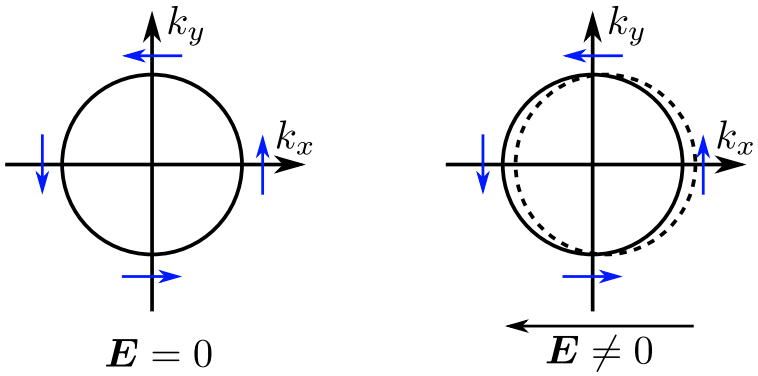

Figure 2.1: Spherical Fermi-surface in two dimensions. The blue arrows indicate the spin-direction according to the Rashba-Edelstein Hamiltonian. An electric field displaces the Fermi-surface in k-space leading to a non-equilibrium spin accumulation.

2.3 Spin-Hall Effect

The spin-Hall effect describes the generation of a spin current $\boldsymbol{j_s}$ perpendicular to a charge current $\boldsymbol{j_c}$ and the spin-polarization direction $\boldsymbol{\sigma}$:

$$\boldsymbol{j_s} = \frac{\hbar}{2\mathrm{e}}\theta_{\mathrm{SH}}\, \boldsymbol{j_c} \times \boldsymbol{\sigma}\ .$$

Here θ_{SH} is the spin-Hall angle and describes the conversion efficiency. In the previous section it was mentioned that spin-orbit coupling in a hydrogen-like atoms is a consequence of the Coulomb interaction (c.f. Eq. (2.3)). In crystals, interactions of the electron with the electrostatic potential of the lattice can lead to similar effects. These scattering events are referred to as extrinsic contributions to the spin-Hall effect. Due to the spin-orbit coupling, the scattering angle of the electron depends on the spin-direction. This gives rise to a spin-current perpendicular to the charge current. These spin-dependent scattering events are usually referred to as *extrinsic contributions* to the spin-Hall effect.

In addition, *intrinsic effects* which do not rely on scattering events but only on the electronic structure can give rise to the spin-Hall effect. This effect is related to the Berry-phase response of the quasi-particles in the solid.

Experimentally, the spin-Hall effect has been detected in semiconductors and heavy metals such as Pt, Ta and W. Different measurement techniques were used to measure to spin-to-charge conversion. This includes direct optical experiments via higher harmonic generation, spin-transport experiments in non-local spin valves, spin pumping experiments and spin-transfer torque experiments.

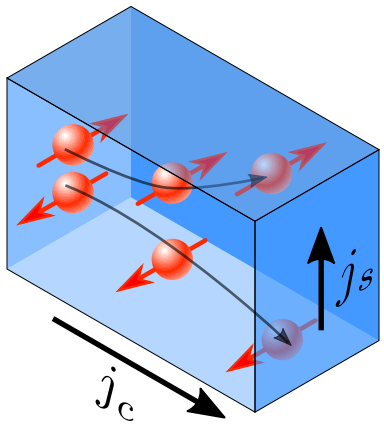

Figure 2.2: Visualization of the spin-Hall effect. A pure spin current $\boldsymbol{j_s}$ is generated perpendicular to the charge current $\boldsymbol{j_c}$ and the spin polarization direction $\boldsymbol{\sigma}$.

2.4 Spin-Orbit Torque

In the previous section the generation of a spin current due to the presence of the Rashba-Edelstein effect or the spin-Hall effect was discussed. If a magnet is in direct proximity to the material with Rashba-Edelstein or spin-Hall effect, the generated spin current can diffuse into the ferromagnet and exert a torque on the ferromagnet. Since materials with large spin-orbit coupling are necessary for the generation of the torque, this phenomenon is referred to as spin-orbit torque.

When electrons diffuse into a ferromagnet and the electron spin is not aligned colinear with the magnetization direction, the electron spin will precess around the magnetization axis. Due to the presence of magnetic damping, the electrons spin will be aligned with the magnetization. In this process the electrons change their angular momentum. Since the total angular momentum of the system must be conserved, the magnetization of the ferromagnet experiences a spin-orbit torque.

The change of angular momentum $\dot{\boldsymbol{L}}$ is equal to a effective torque $\boldsymbol{\tau}_{\text{eff}}$ acting on a system. For a ferromagnet $\boldsymbol{L}$ is proportional to the magnetization $\boldsymbol{m}$, as shown in eqn. (5.3). Therefore, the equation of motion can be written as:

$$\frac{1}{\gamma}\frac{\mathrm{d}\boldsymbol{m}}{\mathrm{d}t} = \boldsymbol{\tau}_{\text{eff}}$$

The effective torque $\boldsymbol{\tau}_{\text{eff}}$ includes contribution from the external magnetic field, the magnetic anisotropy field and spin-orbit torque. The field-like spin-orbit torque $\boldsymbol{\tau}_{\text{fl}}$ is independent of the magnetization and can be written as:

$$\boldsymbol{\tau}_{\text{fl}} = |\boldsymbol{\tau}_{\text{fl}}|\, \boldsymbol{m} \times \boldsymbol{\sigma} = \boldsymbol{m} \times \boldsymbol{B}_{\text{fl}} \,.$$

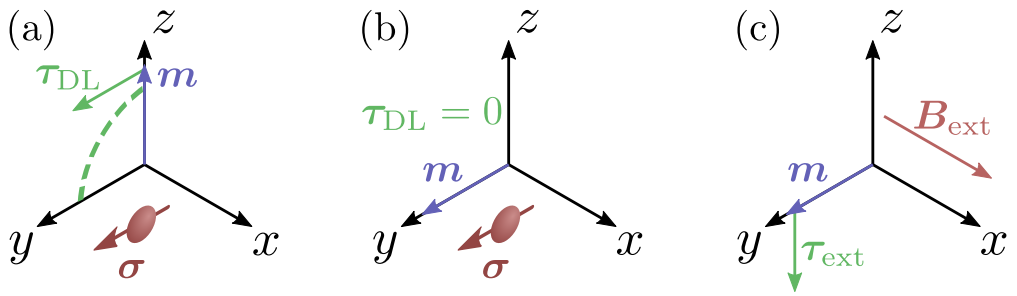

Figure 2.3: (a) Initial configuration with $\boldsymbol{m}$ aligned along the z-direction and $\boldsymbol{\sigma}$ aligned along the y-direction. A torque will be generated along the y-direction and subsequently cause magnetization dynamics. (b) If the torque is sufficiently large, the magnetization will be aligned along the y-direction. However, no deterministic switching occurs since $\boldsymbol{\tau_{DL}}$ is zero if $\boldsymbol{m}$ is parallel to $\boldsymbol{\sigma}$. (c) An in-plane magnetic field $\boldsymbol{B}_{\text{ext}}$ along the x-direction can supply an aditinal torque and lead to deterministic switching.

Here $\boldsymbol{B}_{\text{fl}}$ is the effective field induced by the field-like spin-orbit torque. In addition, damping-like spin orbit torque $\boldsymbol{\tau}_{\text{dl}}$ can be observed:

$$\boldsymbol{\tau}_{\text{dl}} = |\boldsymbol{\tau}_{\text{dl}}|\, \boldsymbol{m} \times (\boldsymbol{\sigma} \times \boldsymbol{m}) = \boldsymbol{m} \times \boldsymbol{B}_{\text{dl}} \; .$$

It is important to notice that the damping-like effective magnetic field $\boldsymbol{B}_{\text{dl}} = |\boldsymbol{\tau}_{\text{dl}}|\boldsymbol{\sigma} \times \boldsymbol{m}$ depends on $\boldsymbol{m}$ itself and is perpendicular to $\boldsymbol{m}$. Thus is can cause magnetization precession and acts like an effective (negative) damping.

Damping-like spin-orbit torque enables magnetization switching, an important application for magnetic memory technologies. The process is outlined in Fig. 2.3. A magnet with out-of-plane magnetic anisotropy is assumed. $\boldsymbol{m}$ is aligned parallel to z and the spin polarization direction is $\hat{y}$. Thus the magnetization will experience spin-orbit torque along $\hat{y}$. Since the change in magnetization is proportional to the torque, $\boldsymbol{m}$ will move along the y-direction. Eventually, $\boldsymbol{m}$ will align parallel to $\hat{y}$ and thus $\boldsymbol{\tau}_{\text{DL}}$ will be zero. In order to archive deterministic switching, an additional torque is needed. This torque can be supplied by an external magnetic field $\boldsymbol{B}_{\text{ext}}$ along the y-direction, as shown in Fig. 2.3(c).

For many applications applying an external magnetic field is not practical. Several solutions exist to avoid external magnetic fields but still archive deterministic switching. These include structural engeneering to tilt the anisotropy axis, the use of antiferromagnets to provide exchange bias or the stray field of in-plane magnetized layers deposited on top or below the magnet to be switched.

For this discussion we assumed single-domain magnets. However, this assumption is only good for nanometer-sized magnets. In larger structures, the magnet will break up into domains during the magnetization reversal process. Under application of spin-orbit torque, domain walls can be moved. The direction of the domain wall motion depends on the alignment of the spins in the domain wall. As a consequence, Neel-type domain walls

will move parallel to the current direction [60] while Bloch-type domain walls will move perpendicular to the current direction [13] in a magnet with out-of-plane anisotropy.

Chapter 3

Electric Transport Characerization of Spin Torque

Electrical transport measurements are an important tool for the characterization of magnetic structures. In the context of this thesis, electric transport refers to the measurement of the longitudinal V_{xx} or transverse voltage V_{xy} under the application of a current and external magnetic field as shown in Fig. 3.1. With the help of transport measurements, various properties of magnetic devices, such as the thermal stability, the spin Hall angle or the switching current can be characterized. In this chapter we will discuss harmonic Hall measurements as to tool to measure effective magnetic fields induced by spin-orbit torque and the unidirectional spin-Hall magneto-resistance. Further, we will discuss current switching experiments that allow determination of the critical current that is required to switch a magnet. Lastly we will discuss field switching experiments that are used to measure the thermal stability of a magnet.

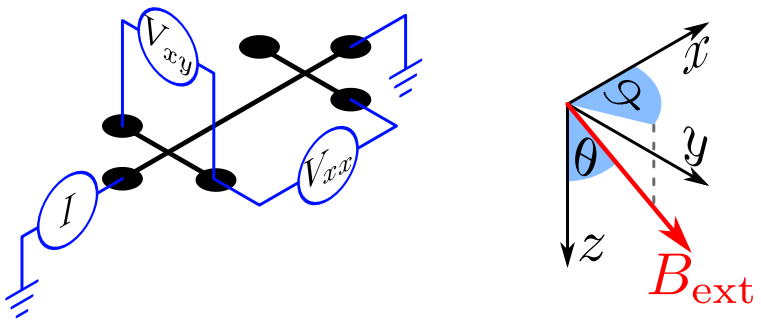

Figure 3.1: The measurements geometry for transport measurements. A current is applied in the x-direction, while the longitudinal (V_{xx}) and transverse voltage (V_{xy}) is measured. In addition, an external magnetic field B_{ext} is applied. The direction of B_{ext} is characterized by the angles θ and φ.

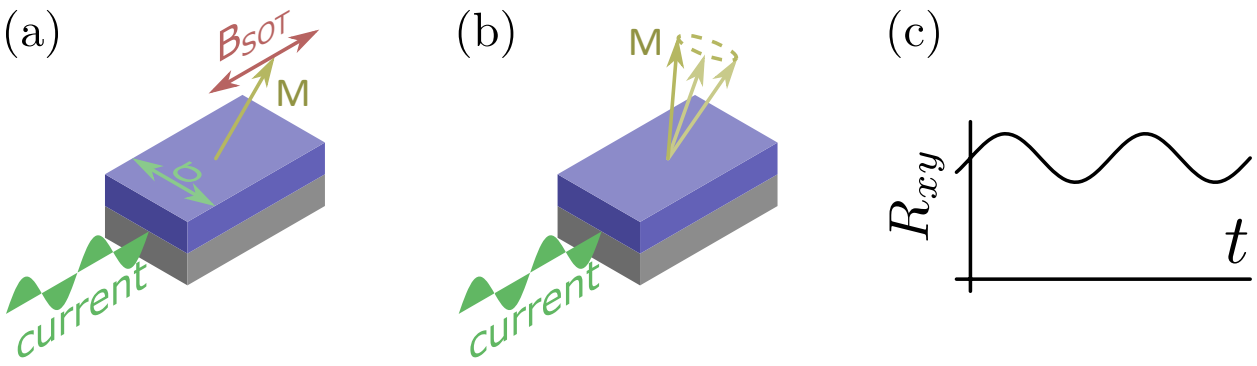

Figure 3.2: (a) An alternating current with frequncy f_{AC} in a heavy metal layer generates a non-equilibrium alternating spin polarization σ at the ferromagnet interface. Through the mechanism of spin-orbit torque, the non equilibrium spin polarization generates a torque on the ferromagnet. The torque can be parameterized as an effective magnetic field B_{SOT}. (b) The torque in the ferromagnet causes magnetization dynamics at the same frequency f_{AC}. (c) Due to magneto-resistive effects in the ferromagnet, the Hall resistance R_{xy} is oscillating with a frequency f_{AC}.

3.1 Harmonic Measurements of Spin-Orbit Torque

In a harmonic measurement, an alternating current is applied to a test device and the voltage is measured at different harmonic frequencies with respect to the base frequency of the current. Within this thesis we are interested in the first and second harmonic voltage. The measurement of the first harmonic longitudinal voltage gives access to a wide range of magneto-resistive effect, including the anisotropic magnetoresistance (AMR), the giant magnetoresistance (GMR), the tunnel magnetoresistance (TMR) and the spin Hall magnetoresistance (SMR). Further, the first harmonic transverse voltage carries signatures of the ordinary Hall effect, the anomalous Hall effect and the planar Hall effect. In order to study non-linear transport effects, the second harmonic voltage is considered. Non-linear effects include spin-orbit torque (SOT), unidirectional spin Hall magnetoresistance (USMR) and thermal effects.

Intuitive Explanation: Harmonic Hall measurements of SOT

If spin-orbit torque is present, an ac current through a heavy metal/ferromagnet heterostructure can generate a Hall voltage at twice the frequency of the applied current. A measurement of this harmonic Hall voltage is used to characterize spin-torque and the spin Hall angle. The mechanism through which a second harmonic Hall voltage is generated can be outlined as follows (c. f. Fig. 3.2):

alternating current	$\xrightarrow{\text{spin torque}}$	magnetization oscillation	$\xrightarrow{\text{magneto-resistance}}$	resistance oscillation	$\xrightarrow{\text{voltage mixing}}$	harmonic voltage

If spin-orbit torque is present, an alternating current $I_{\mathrm{AC}} = I_0 \sin(\omega t)$ can generate a non-equilibrium spin density at the heavy metal / ferromagnet interface. The magnet will experience a torque as a consequence. This torque will cause quasi-equilibrium magnetization oscillations as shown in Fig. 3.2(b). Due to magneto-resistive effects in the magnet, such as the anomalous Hall effect or the planar Hall effect, the Hall resistance will oscillate:

$$R_{xy} = R_{xy}^0 + R_{xy}^{\mathrm{SOT}} \sin(\omega t) \; .$$

Since the resistance, as well as the current are oscillating at the same frequency ω, a second harmonic Hall voltage is generated:

$$\begin{aligned} V_{xy} &= R_{xy} I_{\mathrm{AC}} \\ &= \underbrace{R_{xy}^0 I_0}_{V_{xy}^0} \sin(\omega t) + \underbrace{R_{xy}^{\mathrm{SOT}} I_0}_{V_{xy}^{\mathrm{SOT}}} \sin^2(\omega t) \end{aligned}$$

Using a lock-in amplifier is a convenient way to measure the second harmonic Hall voltage. A lock-in amplifyer will multiply the signal with a reference signal at a fixed frequency and apply a low-pass filter.

$$V_{xy}^{\text{Lock-In}} = \underbrace{\frac{1}{T} \int_0^T \mathrm{d}t}_{\text{low-pass}} \underbrace{\cos(2\omega t)}_{\text{reference}} V_{xy} = \frac{V_{xy}^{\mathrm{SOT}}}{4}$$

This equation holds true for large T. The second harmonic Hall voltage contains a signal due to spin-orbit torque effects.

The general objective is to derive expressions for the amplitude of the spin-orbit torque from a measurement of $V_{xy}^{\text{Lock-In}}$. For this end, two relations have to be derived: First, an expression is needed that relates $V_{xy}^{\text{Lock-In}}$ to the state of the magnetization. Second, an expression is needed that related the state of the magnetization to an abitrary torque that acts on the magnetization. While analytic expressions are know that relate the orientation of the magnetization to the corrsponding Hall resistance, no analyic relation can be derived for the relation between a torque and the magnetization. However, apoximate expressions are known. In the following, approximate experssions for two measurement geometries will be discussed:

- Magnets with in-plane magnetic anisotropy: A magnetic field will be applied along the easy plane of magnetization while the angle of the magnetic field with respect to the current direction will be swept.
- Magnets with perpendicular magnetic anisotropy: An in-plane magnetic field will be applied along a constant direction, but the amplitude of the magnetic field will be swept.

Harmonic Hall measurements with angular sweeps

A convenient way to extract spin-orbit torque induced magnetic fields from harmonic Hall measurement is to study $V_{xy}^{1\omega}$ and $V_{xy}^{2\omega}$ as a function of φ, with $\theta = 90°$ (cf. Fig. 3.1). This technique works well for samples with in-plane magnetic anisotropy since only small magnetic fields are required to saturate the magnetization along the magnetic field direction. Thus, artifacts from anisotropy fields are not expected.

The First Harmonic Voltage

The first harmonic voltage contains information about magneto-transport effects that are linear in current. The transverse voltage $V_{xy}^{1\omega}$, will include contributions from the Hall effect, the planar Hall effect and the anomalous Hall effect. We can write the voltage response in spherical coordinates using the system shown in Fig. 3.1.

$$V_{xy}^{1\omega} = V_{\mathrm{PHE}} \sin(2\varphi_M) \sin^2(\theta_M) + V_{\mathrm{AHE}} \cos(\theta_M) + V_{\mathrm{OHE}} \cos(\theta)$$

Here, V_{PHE} is the amplitude of the planar Hall effect, V_{AHE} is the amplitude of the anomalous Hall effect and V_{OHE} is the amplitude of the ordinary Hall effect. θ is the angle between external magnetic field and current direction and θ_M the angle between the magnetization and the current direction. In all experiments we choose an external magnetic field that is large enough to overcome magnetic anisotropy and saturate the magnetization along the magnetic field direction. Thus $\theta = \theta_M$. It is important to note that the planar Hall effect and the anomalous Hall effect just depend on the magnetization. However, the ordinary Hall effect is proportional to the amplitude of the external magnetic field.

The longitudinal voltage $V_{xx}^{1\omega}$ will contain signals from the anisotropic magnetoresistance (AMR) and the spin-Hall magnetoresistance (SMR). The SMR is a resistive effect that is observed in ferromagnet/heavy metal bilayers and is associated with the spin Hall effect in the heavy metal. We can write the longitudinal voltage as:

$$V_{xx}^{1\omega} = V_{\mathrm{Ohm}} + V_{\mathrm{AMR}} \cos^2(\varphi_M) \sin^2(\theta_M) + V_{\mathrm{SMR}} \sin^2(\varphi_M) \sin^2(\theta_M)$$

Here V_{Ohm} is the ohmic contribution to the resistance, V_{AMR} the amplitude associated with the anisotropic magnetoresistance and V_{SMR} the voltage due to the presence of spin-Hall magnetoresistance.

The Second Harmonic Voltage

The second harmonic voltage contains information about effects that are non-linear in current. Specifically, the transverse voltage $V_{xy}^{2\omega}$ will contain signals from spin-orbit torque

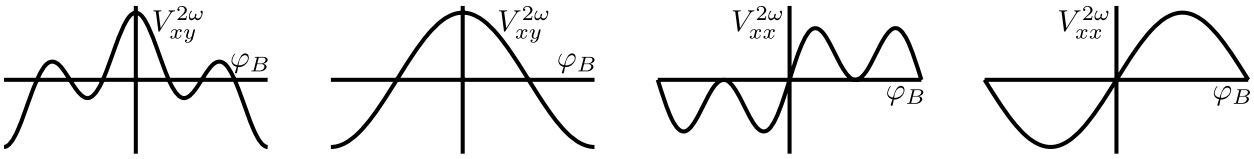

Figure 3.3: Expected angular dependence for $V_{xy}^{1\omega}$ and $V_{xx}^{1\omega}$ if field-like torque, damping-like torque or USMR is present. The range for φ_B spans from $-\pi$ to π. Note that the ordinary Nernst effect and the anomalous Nernst effect have the same angular dependence as dampin-like SOT or USMR respectively.

(SOT) as well as thermal effect.

$$V_{xy}^{2\omega} = \left(\frac{V_{\mathrm{AHE}}}{2} \frac{\Delta B_{\mathrm{DL}}}{B_{\mathrm{ext}} + \mu_0 M_{\mathrm{eff}}} + A\alpha\nabla T + N\alpha B_{\mathrm{ext}} \nabla T \right) \cos(\varphi_{\mathrm{B}}) + \left(V_{\mathrm{PHE}} \frac{\Delta B_{\mathrm{FL}}}{B_{\mathrm{ext}}} \right) \cos(2\varphi_{\mathrm{B}}) \cos(\varphi_{\mathrm{B}}) \, .$$

Here V_{AHE} is the anomalous Hall effect voltage, ΔB_{DL} is the effective field due to the damping like SOT, $\mu_0 M_{\mathrm{eff}}$ is the effective magnetization, A is the coefficient for the ANE/ SSE, α and β are geometrical factors, ΔT is the temperature gradient, N is the ordinary Nernst coefficient and ΔB_{DL} is the effective field due to field-like torque. A measurement of $V_{xy}^{2\omega}$ as a function of φ_B allows for a direct extraction of the field-like SOT. However, it is important to distinguish thermal effect such as the anomalous Nernst effect and the ordinary Nernst effect from the damping-like SOT, since these effects show the same $\cos(\varphi_B)$ angular dependence.

An easy way to archive this, is to consider the scaling of $V_{xy}^{2\omega}$ with external magnetic field. The damping-like SOT is suppressed by external magnetic fields, while the anomalous Nernst effect does not depend on the external magnetic field (but on the magnetization) and the ordinary Nernst effect is enhanced by an external magnetic field.

The longitudinal voltage $V_{xy}^{2\omega}$ can be studied to extract the amplitude of the unidirectional spin-Hall magnetoresistance (USMR). This magneto-resistive effect arises due to a non-equilibrium spin accumulation at a ferromagnet/heavy metal interface. $V_{xy}^{2\omega}$ has the following dependence on φ_B if USMR, thermal effects and field-like SOT are taken into account:

$$V_{xx}^{2\omega} = \left(V_{\mathrm{USMR}} + A\beta\nabla T + N\beta B_{\mathrm{ext}} \nabla T \right) \sin(\varphi_{\mathrm{B}}) + \left(V_{\mathrm{AMR}} \frac{\Delta B_{\mathrm{FL}}}{B_{\mathrm{ext}}} \right) \sin(2\varphi_{\mathrm{B}}) \cos(\varphi_{\mathrm{B}}) \, .$$

Here V_{USMR} is the amplitude of the USMR effect. Note that different contributions to $V_{xx}^{2\omega}$ have different dependence on B_{ext}. Specifically, the USMR has a constant contribution to the harmonic Hall voltage and a field dependent contribution that is suppressed at large

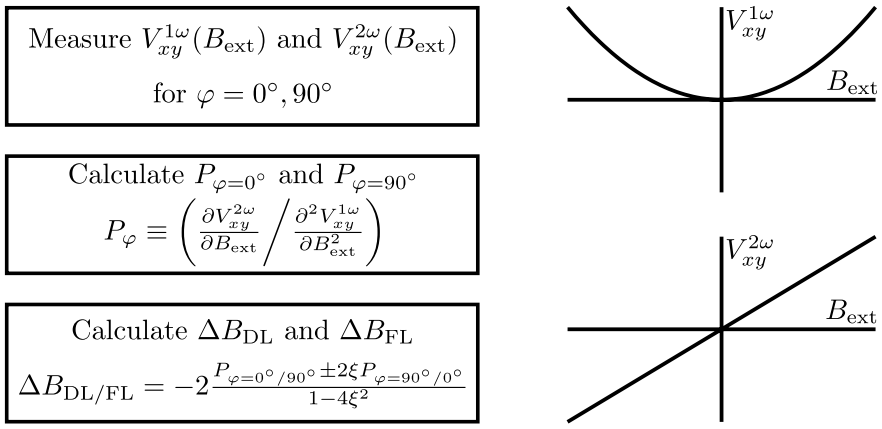

Figure 3.4: Recipe for harmonic Hall measurements of the SOT effective magnetic field for samples with perpendicular magnetic anisotropy. First measure $V_{xy}^{1\omega}$ and $V_{xy}^{2\omega}$ as a function of external magnetic field. Next, calculate P_φ. Finally use P_φ to calculate $\Delta B_{\rm DL/FL}$.

magnetic field. Field-like SOT is suppressed in external magnetic fields, the anomalous Nernst effect does not depend on the external magnetic field and the ordinary Nernst effect is linear.

Harmonic Hall measurements on samples with perpendicular magnetic anisotropy

For samples with perpendicular anisotropy, it is often more convenient to extract spin-orbit torque amplitudes from external magnetic field sweeps along in film plane, parallel or perpendicular to the current direction. The first harmonic voltage as a function of the external magnetic field is written as:

$$V_{xy}^{1\omega} = \pm\frac{V_{\rm AHE}}{2}\left[1 - \frac{1}{2}\left(\frac{B_{\rm ext}\sin(\theta_B)}{\mu_0 H_K \pm B_{\rm ext}\cos(\theta_B)}\right)^2\right]$$

Here $\mu_0 H_K$ is the anisotropy field. The plus/minus sign corresponds to M pointing along the positive/negative z-axis. The second harmonic Hall voltage can be written as:

$$\begin{aligned} V_{xy}^{2\omega} = -\frac{1}{4}\Big[&\mp V_{\rm AHE}(\Delta B_{\rm DL}\cos\varphi + \Delta B_{\rm FL}\sin\varphi) \\ &+ 2V_{\rm PHE}(-\Delta B_{\rm DL}\sin\varphi + \Delta B_{\rm DL}\cos\varphi)\cos 2\varphi\Big] \\ &\times \frac{B_{\rm ext}\sin\theta}{(\mu_0 H_K \pm B_{\rm ext}\cos\theta)^2} \end{aligned}$$

If the first derivative of $V_{xy}^{2\omega}$ with respect to B_{ext} is divided by the second derivative of $V_{xy}^{1\omega}$, the anisotropy field $\mu_0 H_K$ cancels out. We call the expression P_φ:

$$P_\varphi \equiv \left(\frac{\partial V_{xy}^{2\omega}}{\partial B_{\text{ext}}} \Big/ \frac{\partial^2 V_{xy}^{1\omega}}{\partial B_{\text{ext}}^2}\right) = -\frac{1}{2}\left[\left(\Delta B_{\text{DL}} \mp 2\frac{V_{\text{PHE}}}{V_{\text{AHE}}}\Delta B_{\text{FL}} \cos 2\varphi\right)\cos\varphi + \left(\Delta B_{\text{FL}} \pm 2\frac{V_{\text{PHE}}}{V_{\text{AHE}}}\Delta B_{\text{DL}} \cos 2\varphi\right)\sin\varphi\right]$$

Next, two explicit values for φ are chosen. Further, we call $\xi = V_{\text{PHE}}/V_{\text{AHE}}$:

$$P_{\varphi=0} = \frac{1}{2}\left(\Delta B_{\text{DL}} \pm 2\xi\Delta B_{\text{FL}}\right)$$
$$P_{\varphi=90} = \frac{1}{2}\left(\Delta B_{\text{FL}} \pm 2\xi\Delta B_{\text{DL}}\right)$$

These equations can be solved for ΔB_{DL} and ΔB_{FL}:

$$\Delta B_{\text{DL}} = -2\frac{P_{\varphi=0} \pm 2\xi P_{\varphi=90}}{1-4\xi^2}$$
$$\Delta B_{\text{FL}} = -2\frac{P_{\varphi=90} \pm 2\xi P_{\varphi=0}}{1-4\xi^2}$$

With these two expressions a harmonic Hall measurement to extract ΔB_{DL} and ΔB_{FL} is straightforward. $V_{xy}^{1\omega}$ and $V_{xy}^{2\omega}$ as a function of B_{ext} can be extracted from magnetic field sweeps along the x- and y-axis. Next, it is possible to calculate $P_{\varphi=0}$ and $P_{\varphi=90}$. The values obtained here can be used in the expression above to calculate the effective magnetic fields due to SOT. This procedure is summarized in Fig. 3.4.

Measurement Setup for Harmonic Measurements

As outlined above, the measurement task for harmonic Hall measurements is to record harmonic voltages as a function of a set of control parameters. In our studies, these control parameters include the amplitude of the applied current, the amplitude of the external magnetic field and the angle at which the external magnetic field is applied. Figure 3.5 shows a schematic overview of the experimental setup.

An AC current is applied by a *Keithley 6221A* current source. The sample is mounted in a *Bruker ESR magnet* that can apply a maximum of 1 T magnetic field. Further, the sample can be rotated with an *Applied Motion ST5-S* drive and *HT17-075* stepper motor. The voltage response of the DUT is recorded with a *Signal Recovery 7270* lock-in amplifier. The monitor output of the lock-in amplifier provides the amplified signal to a *National Instruments 6341* I/O device, where a time-trace is recorded. The data recorded by the lock-in amplifier is directly stored by a computer. The time-traces recorded from the I/O device are processed on the computer to extract the harmonic Hall voltages using fast Fourier

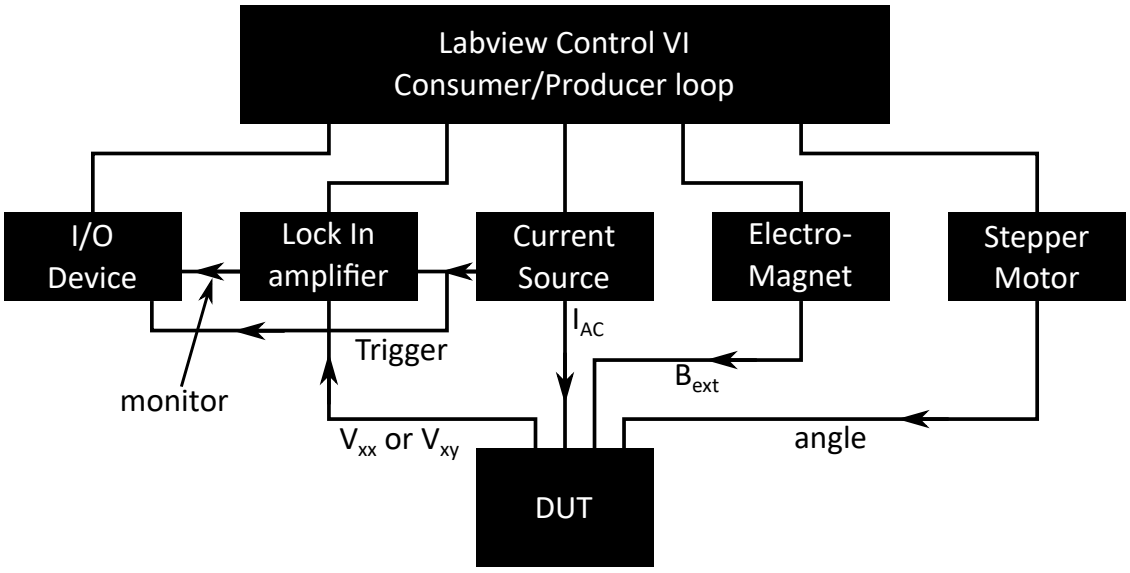

Figure 3.5: Schematic of the harmonic Hall measurement setup. A Labview VI is used to control the current I_{AC}, the external magnetic field B_{ext} and the angle at which B_{ext} is applied. The voltage V_{xx} or V_{xy} is measured with a lock-in amplifier. In addition, the real time signal is recorded with a multifunction I/O device. The current source provides a trigger signal for the lock-in amplifier and the I/O device.

transformation. The trigger link from the *Keithley 6221A* current source is used to provide a trigger signal for the *Signal Recovery 7270* lock-in amplifier and the *National Instruments 6341* I/O device. The *LabVIEW* programming enviroment is used to control the setup and handle the data processing.

3.2 Current Induced Magnetization switching

Current switching experiments of magnets with perpendicular magnetic anisotropy are performed to measure the critical current that is required to switch a magnet with the help of spin-orbit torque. For spin-orbit torque switching, in-plane magnetic fields are required to break the symmetry. Typically, switching phase diagrams are recorded, where the critical switching current is plotted as a function of the applied in-plane magnetic field.

The setup for current switching experiments is outlined in Fig. 3.6. The in-plane magnetic field is applied by an electromagnet. A Gaussmeter (*Lake Shore 475 DSP*) and a PI-control loop is used to set the magnetic field to the desired value. Current pulses are applied to the DUT with a *Keithley 6221A* and the anomalous Hall voltage is recorded with a *Keithley 2182A* nanovolt meter. The current source provides a trigger signal for the nanovolt meter. The pulsed delta measurement mode is used to perform this measurement.

In addition, the sample can be rotated in the magnetic field with an *Applied Motion ST5-*

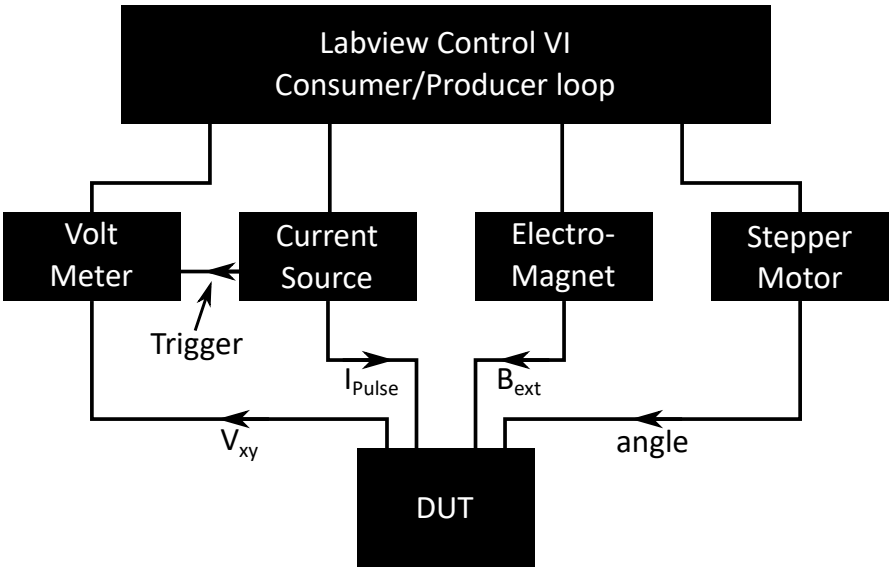

Figure 3.6: Schematic of the pulse switching setup. An electromagnet is used to apply in-plane magnetic field to break the symmetry. Current pulses are applied and the anomalous Hall voltage (indicating the state of the magnetization) is detected with a voltmeter. A stepper motor can be used to rotate the samples. This is necessary to apply out-of-plane magnetic field to reset the magnet.

S drive and *HT17-075* stepper motor to apply out-of-plane magnetic field. This is necessary to reset the magnet into a defined state with an out-of-plane magnetic field.

3.3 Thermal Stability Characterization

The critical switching current alone does not suffice to evaluate the usefulness of magnetic devices for memory applications. In addition to small switching currents, a large thermal stability is important. In this thesis we use field switching experiments to determine the thermal stability of spin-orbit torque devices. In these experiments, the anomalous Hall effect is used to probe the state of magnetization while an external magnetic field is used to switch the magnet. The coercive field of the magnet depends on the rate at which the external magnetic field is swept. The thermal stability can be extracted from this sweep rate dependence.

Magnetization switching is a thermally activated process. The faster the magnetic field is swept, the lower will be the probability that a switching event occurs at a given magnetic field. By measuring the dependence of the coercive field H_C on the sweeping rate, the thermal

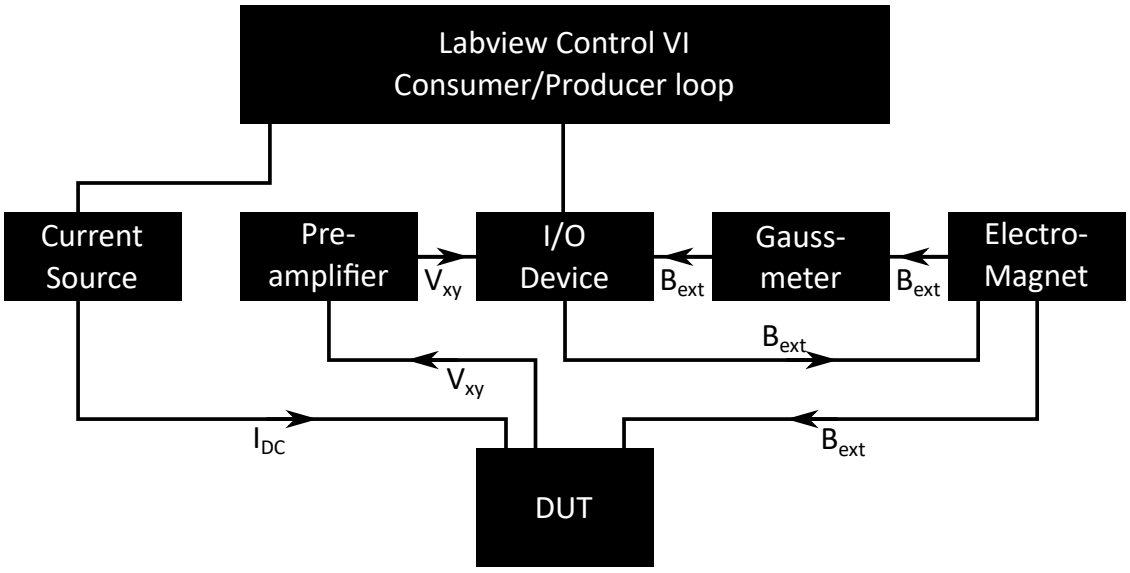

Figure 3.7: Schematic of the thermal stability setup. A small DC current is applied to the DUT while the anomalous Hall effect voltage is first amplified and then detected with an AD converter. Simultaneously, an analog signal from the gaussmeter is detected. The I/O device also controls the magnetic field supplied by the electromagnet.

stability Δ can be extracted. The following model by El-Hilo *et al.* is used:

$$H_C = H_K \left(1 - \sqrt{\frac{1}{\Delta} \ln \left[\frac{f_0 H_K}{2\Delta} \frac{1}{r}\right]}\right)$$

Here, H_K is the anisotropy field, f_0 the attempt frequency and r the sweeping rate.

The experimental setup to measure H_C as a function of r is outlined in Fig. 3.7. A *Keithley 6221A* current source is used to apply a DC current to the sample. The magnetization state is probed by recording the anomalous Hall voltage. V_{xy} is amplified with a *Stanford Research 560* amplifier and recorded with a *National Instruments 6341* I/O device. The magnet is driven by a *Kepco BOP 20-20* power supply. An analog voltage signal from the *National Instruments 6341* is used to control the sweep rate of the magnetic field. The magnetic field is measured with a *Lake Shore 475 DSP* gauss-meter and recorded with the *National Instruments 6341* I/O device. The magnetic field and the anomalous Hall voltage are recorded simultaneously at a high rate. Due to the stochastic nature of the switching event it is essential to record several switching switching cycles at any given sweep rate.

Chapter 4

Spin-Orbit Torque in RE-TM Ferrimagnets

4.1 The Role of the Magnetic Sublattice

The spin-orbit torque switching of ferrimagnetic $Gd_x(Fe_{90}Co_{10})_{100-x}$ films was studied for both transition metal (TM)-rich and rare earth (RE)-rich configurations. The spin-orbit torque driven magnetization switching follows the same sense in TM-rich and RE-rich samples with respect to the total magnetization, but the sense of the switching is reversed with respect to the TM magnetization. This indicates that the sign of the spin-orbit-torque-driven magnetic switching follows the total magnetization, although transport based techniques such as anomalous Hall effect are only sensitive to the transition metal magnetization. These results provide important insight into the physics of spin angular momentum transfer in materials with antiferromagnetically coupled sublattices.

4.2 Magnetic coupling in ferrimagnetic GdFeCo

Magnetization dynamics at interfaces has been investigated extensively over the last three decades [49, 103, 11]. In that context 'spin-orbit torque' (SOT) has received a lot of interest recently. Here, a charge current in a heavy metal is converted into a spin current via spin-orbit coupling and injected into an adjacent ferromagnet [65, 67, 79, 77]. The transfer of angular momentum from the spins to the ferromagnet causes a torque on the magnetization which can switch the magnet [79, 77]. To date, most studies of SOT have concentrated on $3d$ ferromagnets such as Co [65, 79, 43, 118] FeCo [26], FeCoB [38, 90, 28], FePd [57] or transition metal rich ferrimagnetic alloys such as TbFeCo [126]. Here we report SOT switching of ferrimagnetic GdFeCo alloys with both rare earth (RE) rich or transition metal (TM) rich configurations with bulk perpendicular magnetic anisotropy (PMA) at room temperature.

Our study is based on $Gd_x(Fe_{90}Co_{10})_{100-x}$ thin films, where the antiferromagnetic ordering between Gd $4f$ and FeCo $3d$ magnetic moments is mediated by Gd 5d electrons via

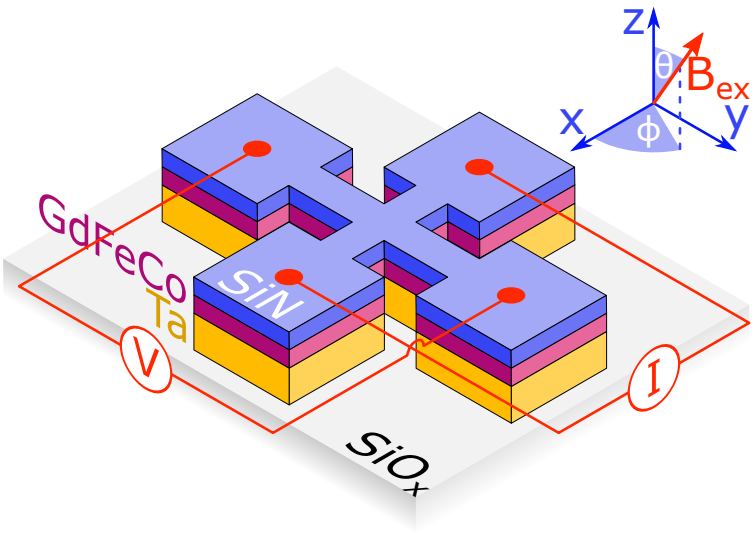

Figure 4.1: Schematic of the measurement geometry used for SOT measurements. The samples are Ta/a-GdFeCo/a-SiN films, where the a-GdFeCo layer exhibits perpendicular magnetic anisotropy. Films are patterned into Hall bar structures for transport measurements. A current is applied along the x-direction while the anomalous Hall effect voltage is measured along the y-direction. An external magnetic field can be applied to the sample.

$4f$-$5d$ exchange interaction and $3d$-$5d$ hybridization [15, 89] and indirect RKKY conduction band exchange. The magnetic properties of $Gd_x(Fe_{90}Co_{10})_{100-x}$ can be varied by changing the composition x. A comparison between TM-rich and RE-rich samples allows us to conclude that the anomalous Hall effect (AHE) changes sign for these two different samples, in accordance with literature [3, 73, 78, 101], while the SOT-driven magnetic switching has the same sign in both samples. Further, the effective magnetic fields, induced by damping-like and field-like SOT, do not show any change in the sign.

4.3 Sample growth and fabrication

Ta(10)/$Gd_x(Fe_{90}Co_{10})_{100-x}$(5)/Si-N(5) films (thickness in nm) were grown by RF magnetron sputtering on thermally oxidized silicon substrates with compositions $x = 21$ (TM-rich) and $x = 28$ (RE-rich). The base pressure during deposition was lower than 1×10^{-8} Torr. The SiN overlayer is used to prevent oxidation. After growth, PMA was confirmed with magnetometry. Hall bar mesa structures with a width of 20 µm were patterned using optical lithography and ion milling. The layout of the sample and the measurement setup are shown in Fig. 4.1. DC or AC currents are applied along the x-direction while the transverse voltage is measured. The orientation of the external magnetic field B_{ex} is defined by spherical coordinates ϕ and θ. This device structure is used for AHE and planar Hall effect (PHE) measurements. We find that the resistivity of our samples is $\rho_{TM} = 320\,\mu\Omega\,cm$ and $\rho_{RE} =$

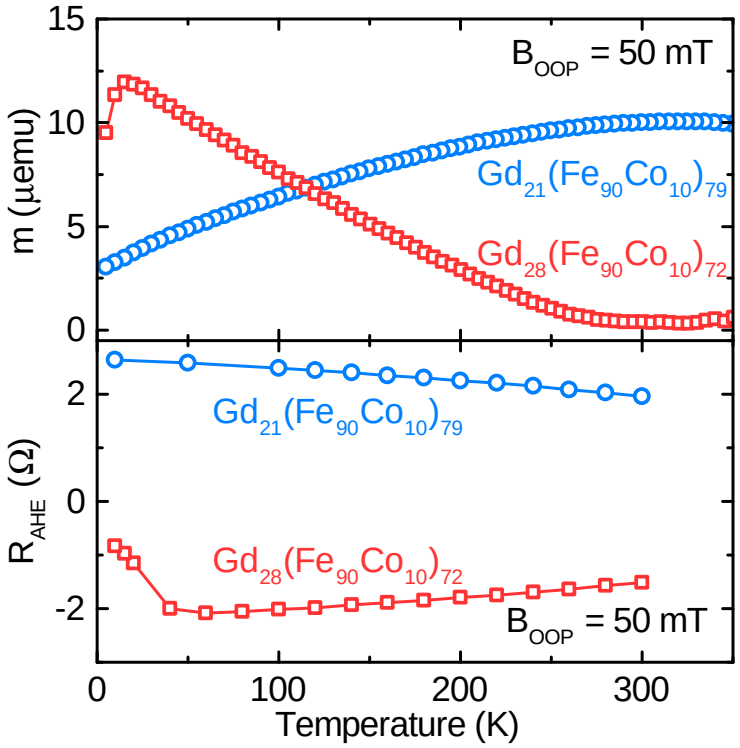

Figure 4.2: The anomalous Hall resistance as a function of temperature is plotted for the TM-rich sample (blue circles) and the RE-rich sample (red squares). The measurements are taken with an applied out-of-plane field B_{OOP} of 50 mT. The investigated samples show no compensation point below room temperature.

342 μΩ cm for the TM-rich and the RE-rich sample respectively.

4.4 The anomalous Hall effect

Using SQUID magnetometry, the magnetization as a function of temperature was studied for both TM-rich and RE-rich samples. The result is shown in Fig. 4.2. In the TM-rich sample, m is increasing with increasing temperature. As the temperature is increased the magnetization of both sublattice magnets is decreasing. However, the Gd magnetization will decrease faster. Since the TM is dominant in the TM-rich sample, the total magnetic moment increases. On the other hand, the total magnetization in the RE-rich samples decreases due to the strong temperature dependence of the Gd magnetization.

The AHE of GdFeCo as a function of temperature is shown in Fig. 4.2. An out-of-plane magnetic field of $B_{\mathrm{OOP}} = 50$ mT is applied to fix the magnetization and prevent domain nucleation. The AHE resistance is proportional to the out-of-plane component of the TM magnetization [3, 73, 78, 101]. In the RE-rich sample, the transition metal moment is aligned

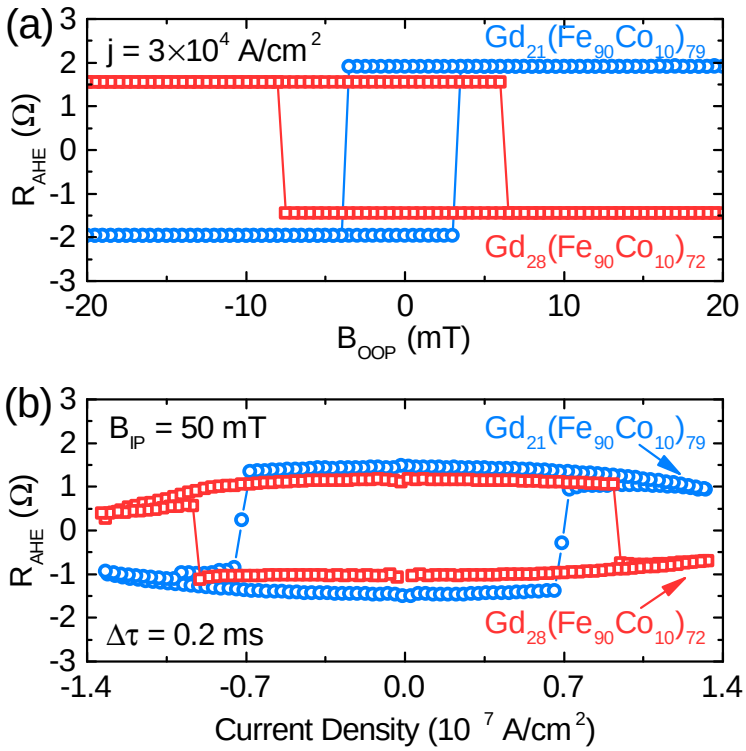

Figure 4.3: **(a)** Anomalous Hall resistance at room temperature as a function of out-of-plane magnetic field B_{OOP}. The sign of the anomalous Hall effect is different in the TM-rich and RE-rich samples. **(b)** Spin-orbit-torque-driven switching of the magnetization. A magnetic field of 50 mT is applied parallel to the current direction to break the symmetry. The current pulse width is $\Delta\tau = 200\,\mu\mathrm{s}$. The sign of the SOT-driven switching is the same in both samples.

antiparallel to the external magnetic field and thus a negative AHE resistance is measured. Since the AHE resistance does not change sign over the whole measurement range, there is no compensation point for the magnetization in either our samples. The small decrease in AHE resistance (R_{AHE}) as a function of temperature, seen in both samples, is due to a decrease of the saturation magnetization in the TM. The decrease of R_{AHE} at temperature below 50 K in the RE-rich sample is due to a change of the magnetic anisotropy where the in-plane anisotropy field becomes comparable to $B_{\mathrm{OOP}} = 50\,\mathrm{mT}$ and thus tilts the magnetization from out-of-plane to in-plane. This is because the net magnetization of the sample has grown large (due to Gd moment increasing more rapidly than TM moment with decreasing temperature) causing dipolar coupling energy to become larger than perpendicular anisotropy energy.

After confirming that the magnetization of $\mathrm{Gd}_x(\mathrm{Fe_{90}Co_{10}})_{100-x}$ is dominated by the TM magnetic moment for $x = 21$ and by the RE magnetic moment for $x = 28$, we concentrate on room temperature measurements. Figure 4.3(a) shows the anomalous Hall voltage as a function of the external magnetic field applied along the easy axis of the magnet ($\theta = 0$).

The current density is small to avoid heating- and SOT-induced effects. Sharp switching in this measurement indicates good PMA. The RE-rich sample shows a higher coercive field because it is closer to the compensation temperature. As mentioned earlier, the AHE has opposite sign for the TM-rich sample and RE-rich sample because it is proportional to the out-of-plane component of the TM. This leads to the different sense of the hysteresis loops.

4.5 Spin-orbit torque switching

The SOT-induced switching of the magnetization is shown in Fig. 4.3(b). During the measurement a 50 mT in-plane magnetic field with $\phi = 0$ and $\theta = \pi/2$ is applied to break the symmetry. 200 µs long current pulses are used to switch the magnetization. Consider the TM-rich sample first: If we call the negative AHE resistance state down (because that is the equilibrium state if a large negative magnetic field is applied along the easy axis), then a positive current pulse will switch the total magnetization from down to up. In the RE-rich sample we call the positive AHE resistance state down (again, this is the equilibrium state if a negative magnetic field is applied along the easy axis). A positive current pulse will then switch the total magnetization of the RE-rich sample from down to up, *just as it did for TM-rich sample*. Thus, SOT-driven magnetic switching follows the same sense in both samples with respect to the total magnetization (down $\rightarrow$ up for positive current pulses). However, SOT-driven switching has a different sign in TM- and RE-rich samples with respect to the FeCo magnetization as measured by the AHE and thus the sense of the hysteresis is different in both samples as shown in Fig. 4.3(b).

4.6 Harmonic Hall measuremets of spin-orbit torque

Next we performed harmonic Hall voltage measurements following Hayashi *et al.* [38] to characterize the effective magnetic fields induced by SOT. To this end, an AC current with $\omega = 97$ Hz is applied to the sample and the first- and second harmonic voltage responses (V_ω and $V_{2\omega}$) are measured. To measure the Slonczewski-like SOT H_{SL}, an external magnetic field is applied parallel to the current direction, while the magnetic field is applied perpendicular to the current to measure the field-like SOT H_{FL}. The field is swept quasistatically between ± 60 mT. During the measurement, a small out-of-plane field (≈ 5 mT) is applied to prevent the magnet from breaking into domains. The effective fields can be calculated using the following procedure:

$$H'_{\mathrm{SL,FL}} = \left(\frac{\partial V_{2\omega}}{\partial H_{\mathrm{SL,FL}}}\right) \times \left(\frac{\partial^2 V_\omega}{\partial H^2_{\mathrm{SL,FL}}}\right)^{-1}, \tag{4.1}$$

$$H_{\mathrm{SL,FL}} = -2\frac{H'_{\mathrm{SL,FL}} \pm 2\xi H'_{\mathrm{FL,SL}}}{1 - 4\xi^2}. \tag{4.2}$$

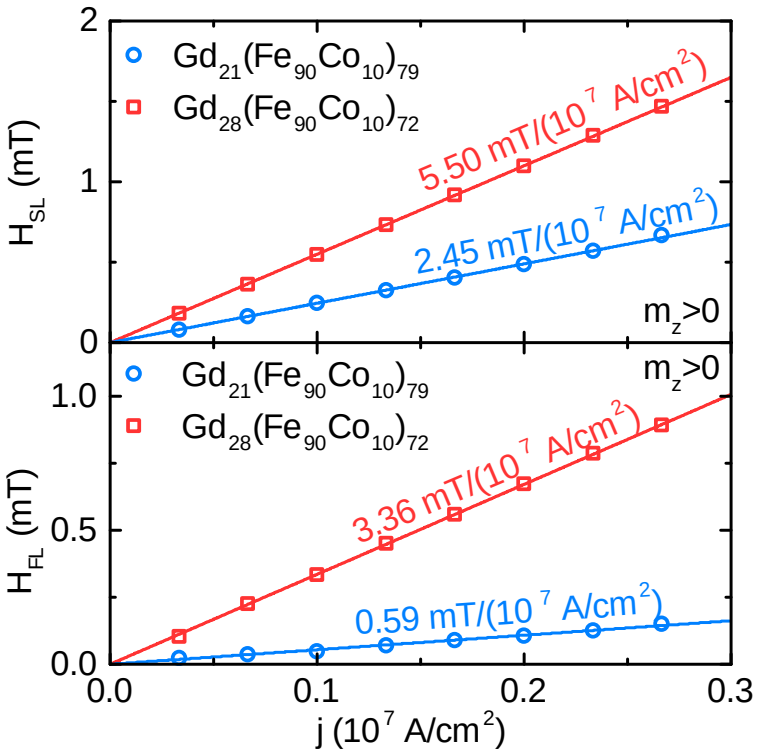

Figure 4.4: The upper panel shows the longitudinal effective field as a function of the current density in the Ta layer for the TM-rich and the RE-rich sample while the lower panel shows the transverse effective field. The solid lines are fits to the experimental data. All measurements were taken with an out-of-plane field of $\approx 5\,\mathrm{mT}$ to ensure $m_z > 0$.

Here V_ω and $V_{2\omega}$ are the first and second harmonic Hall voltages, respectively. The plus (minus) sign in eqn. (4.2) applies to m pointing along the positive (negative) direction. ξ is the ratio of planar Hall effect and anomalous Hall effect: $\xi = \Delta R_{\mathrm{PHE}}/\Delta R_{\mathrm{AHE}}$. In our samples we find $\xi_{\mathrm{TM}} = 0.072$ for the TM-rich sample and $\xi_{\mathrm{RE}} = 0.069$ for the RE-rich sample, measured via in-plane rotations of the magnetic field: $R(\phi)$ at $\theta = \pi/2$.

The effective damping field is shown in the upper panel of Fig. 4.4. For both samples, the fields are a linear function of the current density. This linear relationship also shows that heating does not play a role in these measurements. The data was recorded for m pointing along the positive z-direction. However it was confirmed that the Slonczewski field changes sign for m pointing along the negative z-direction. The effective fields for the TM-rich and the RE-rich sample have the same sign, which is in agreement with the switching measurements reported earlier. It is important to notice that the effective damping field in the RE-rich sample is twice as large in magnitude as in the TM-rich sample at a given current density. The lower panel of Fig. 4.4 shows the field-like (FL) torque. The field-like torque follows the same trend in that it is smaller for the TM-rich sample. It was confirmed that the FL-torque does not change sign for $m_z < 0$ for both samples.

4.7 Angular momentum transfer in TM/RE magnets

Mechanisms for the anomalous Hall effect discussed in literature include Berry phase [85, 52, 8], side-jump scattering [12] and screw scattering [104, 82]. This indicates that the AHE is ultimately a conduction electron effect. According to Hund's rules Gd has a large magnetic moment due to a half filled $4f$-shell; the f-shell is localized and does not contribute to conduction (except by scattering of conduction electrons). In Fe, however, the d-band is spin-split and thus the conduction electrons are spin polarized. For that reason we expect the AHE to be dominated by the TM conduction electrons and consequently to follow the sign of m_{TM} as seen in the experiments described above.

SOT, on the other hand, is an angular momentum transfer process. Due to a current in the Ta, electrons of one spin species will diffuse into the adjacent GdFeCo layer. This spins lie along the $\hat{y}$-axis and are not collinear to the magnetization vector in the magnet and thus they are not eigenstates. Therefore they will begin to precess around the magnetization axis. Due to the presence of damping, the electron spin will eventually align with the magnetization and average out within the spin coherence length [56]. If angular momentum is conserved in the system, there needs to be an angular momentum transfer process from the injected electrons to the magnetization of the ferromagnet. The change of the angular momentum (eg. the torque) is of the form $\boldsymbol{\tau} = \tau_0 \boldsymbol{m} \times (\boldsymbol{\sigma} \times \boldsymbol{m})$, where $\boldsymbol{\sigma}$ is the spin polarization [14].

Given the localized nature of the 4f spins in Gd, it is natural to expect that the spin angular momentum transfer will happen predominantly with the 3d spins of CoFe and therefore the switching will be determined by the CoFe magnetization much like how AHE is determined by the magnetization of CoFe. However, we find that the sign of the switching depends on the net magnetization and not only on the magnetization of TM sub-lattice. The result is consistent with spin torque measurements in GMR spin vales, where the sign of the GMR effect changes for TM- and RE-rich samples, but the sign for spin-torque switching remains unchanged [48].

It should be noted that in addition to a magnetization compensation point, an angular momentum compensation point has been observed in GdFeCo thin films due to the different gyromagnetic ratios of the Gd and FeCo sublattices [106]. However, angular momentum compensation does not play a role in our experiments with the RE-rich sample as the angular momentum compensation temperature is above the magnetization compensation temperature. The TM-rich sample is far away from compensation.

In conclusion we have studied SOT in Ta/GdFeCo/SiN structures with PMA. It was shown by temperature dependent measurements that the AHE is proportional to the out-of-plane magnetization of the transition metal. The spin-orbit-torque-driven magnetization switching follows the same sense in TM-rich and RE-rich samples with respect to the total magnetization, but the sense of the switching is reversed with respect the to TM magnetization. Therefore, we conclude that the angular momentum transfer process due to SHE in Ta has the same sign in both magnetic sub-systems, FeCo and Gd. In addition, 2ω measurements confirm that the effective fields induced by spin-orbit torque have the same sign in both samples. However, the effective field induced in the RE-rich sample is twice as large

as in the TM-rich sample, even bigger than effective fields observed in Ta/CoFeB samples.

Chapter 5

Thickness scaling of Spin-Orbit Torque

We report on spin-orbit torque (SOT) measurements in amorphous ferrimagnetic $Gd_{21}(Fe_{90}Co_{10})_{79}$ films with bulk perpendicular magnetic anisotropy (PMA) and thicknesses up to 30 nm. The damping-like and field-like torques have been quantified using second harmonic Hall voltage detection. Both torques show an inverse linear dependence on the thickness that is indicative of the interfacial nature of the torques. The spin-Hall angle remains constant over the thickness range of 10 nm to 30 nm $Gd_{21}(Fe_{90}Co_{10})_{79}$. Remarkably, we find that this interfacial torque is able to switch a 30 nm thick $Gd_{21}(Fe_{90}Co_{10})_{79}$ film with a reasonably large thermal stability of $\approx$100 k_BT.

5.1 Bulk Magnetic Anisotropy and Thickness Scaling

Spin-orbit torque (SOT) devices have received attention recently due to their potential impact on next generation memory technology [61, 29]. Here SOT refers to the generation of a non-equilibrium spin-accumulation at a heavy metal (HM)/ferromagnet (FM) interface, either due to the bulk spin-Hall effect in the HM [67, 65] or the Rashba-Edelstein effect at the HM/FM interface [79]. This non-equilibrium spin-accumulation diffuses into the ferromagnet [37], where it can reverse the magnetic order via the spin-transfer torque mechanism [11, 103].

In most SOT studies, as of today, transition metal magnets, such as Co or Fe with MgO capping layers, are used [45]. Here, the perpendicular magnetic anisotropy (PMA) originates from hybridization effects at the ferromagnet/oxide interface[120]. Due to the inherent interfacial nature of this anisotropy, the ferromagnetic films must be grown very thin (on the order of a 1 nm)and the Co/MgO must be clean and have the right oxygen stoichiometry. This imposes a fundamental bottleneck on the scaling of SOT devices, because it results in a reduction of thermal stability if the area of these devices is reduced.

One way to overcome this problem is to use magnetic materials with bulk PMA [41], where the effect of decreasing footprint area can be compensated by increasing the thickness of the magnet. Indeed, SOT switching has recently been investigated in HM/ferrimagnet

structures with bulk PMA, where the ferrimagnets are transition metal (TM)-rare earth (RE) alloys [126, 111, 112, 96, 30, 80, 35].

So far, however, a detailed study of the thickness dependence of SOT in magnets with bulk PMA is still lacking in literature. Such a study is important for two reasons: first, the thickness dependence of the torque components can shed light onto the underlying physics of SOT itself; secondly, the thickness dependence of the film is relevant for memory applications, due to the potential for scaling. It should be noted that previous studies of the thickness dependence of SOT in magnets with bulk PMA were limited to ultra thin magnetic films of just a few nanometers thickness due to changes in the crystalline structure with thickness [57].

In the work presented here, we have investigated the thickness dependence of SOT in ferrimagnetic $Gd_{21}(Fe_{90}Co_{10})_{79}$ films. We vary the thicknesses from 10 nm to 30 nm and show that all films can be switched with 200 µs current pulses through adjacent HM layers. To measure the effective magnetic field due to SOT we perform harmonic Hall measurements. The effective field is found to be inversely proportional to the ferrimagnet film thickness and saturation magnetization. In addition, field switching experiments are performed to measure the thermal stability. It is found that the critical switching current j_c, as well as the thermal stability Δ, increase linearly with thickness, so that the switching efficiency j_c/Δ is constant.

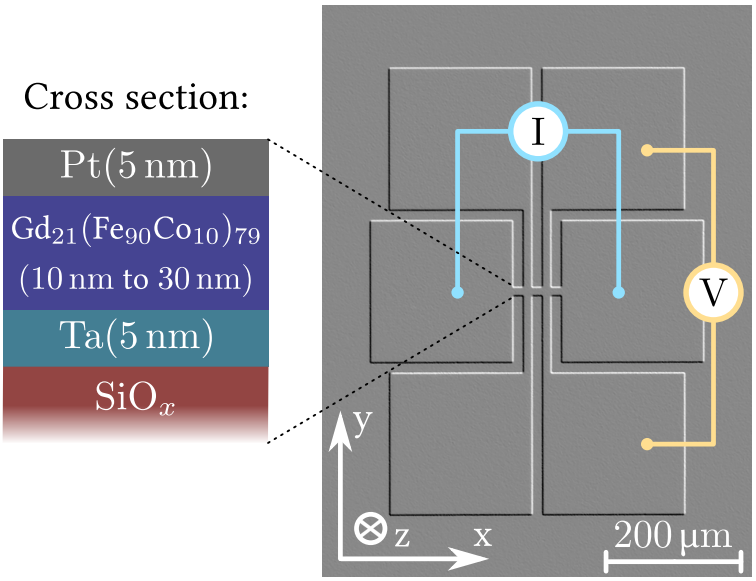

Figure 5.1: Microscope image of a Hall bar device. Transition metal rich Ta(5)/ $Gd_{21}(Fe_{90}Co_{10})_{79}(t)$/Pt(5) (thickness in nm) structures are investigated. A current is applied along the x-direction and the Hall voltage is detected along the y-direction. The width of the Hall bar is 20 µm.

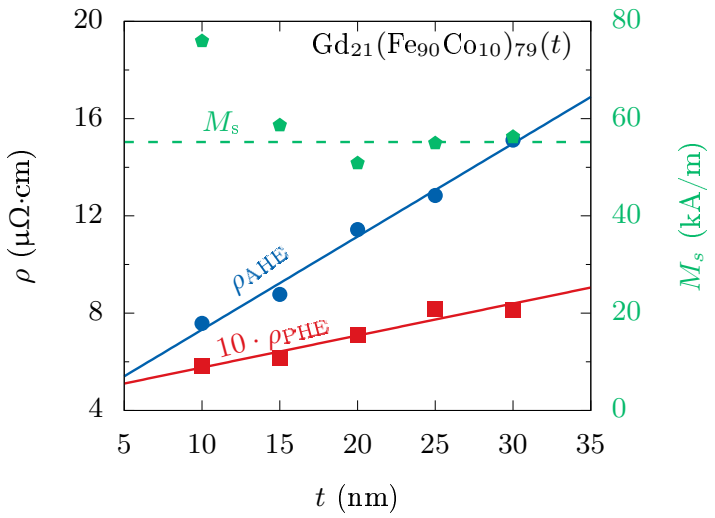

Figure 5.2: The AHE resistivity ρ_{AHE} (blue, left axis) as well as the PHE resistivity ρ_{PHE} (red, left axis) depend linearly on the $Gd_{21}(Fe_{90}Co_{10})_{79}$ thickness. The saturation magnetization was measured with VSM magnetometry and is plotted in green on the right axis. M_{S} is constant for samples with thickness $t > 10\,\mathrm{nm}$. At $t = 10\,\mathrm{nm}$, the magnetization is enhanced.

5.2 Sputter Deposition of GdFeCo

We deposited a series of $\mathrm{Ta}(5)/Gd_{21}(Fe_{90}Co_{10})_{79}(t)/\mathrm{Pt}(5)$ films (thickness in nm) on thermally oxidized silicon substrates by RF magnetron sputtering. The thickness t was varied from 10 nm to 30 nm in steps of 5 nm. The base pressure during deposition was below 1×10^{-8} Torr. After deposition, Hall bar mesa structures were defined by optical lithography and Ar-ion milling. Figure 5.1 shows an optical image of a typical Hall bar device and the measurement geometry. The width of the Hall bar is 20 μm. A current is applied along the x-direction to excite SOT dynamics. The response of the magnet is detected by the AHE, measured perpendicular to the current direction, along y. Note that $Gd_{21}(Fe_{90}Co_{10})_{79}$ is a transition metal rich alloy with $|m_{\mathrm{TM}}| > |m_{\mathrm{RE}}|$. The resistivity of the $Gd_{21}(Fe_{90}Co_{10})_{79}$ is $\rho = 1.19\,\mathrm{m\Omega\,cm}$.

5.3 Spin-Orbit Torque Induces Effective Fields

$Gd_{21}(Fe_{90}Co_{10})_{79}$ is a TM-RE alloy, with antiferromagnetic coupling between the TM and RE magnetic moments [18]. The anomalous Hall effect (AHE) in TM-RE ferrimagnets is proportional to the out-of-plane component of the TM magnetization, while the RE magnet does not contribute significantly the the AHE [101, 78]. This is because the conduction electrons in the TM are spin polarized while the RE has no spin-split conduction band.

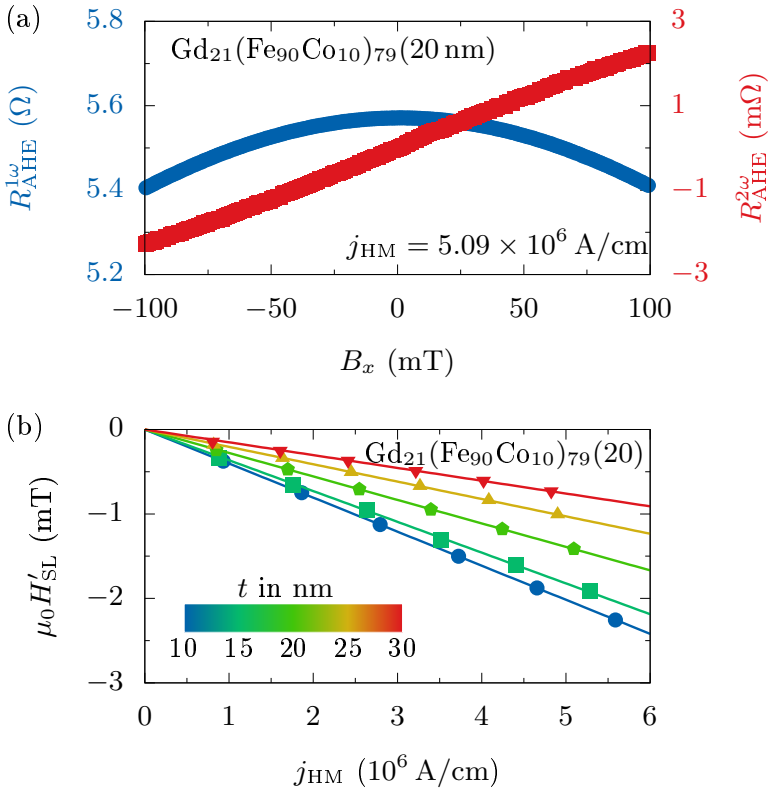

Figure 5.3: Harmonic Hall measurement of the effective magnetic field induced by SOT. Panel (a) shows the first- and second harmonic Hall resistance as a function of in-plane magnetic field B_x parallel to the current direction for a 20 nm thick $Gd_{21}(Fe_{90}Co_{10})_{79}$ film. From this measurement the Slonczewski effective field $\mu_0 H_{SL}$ can be extracted. Panel (b) shows that $\mu_0 H'_{SL}$ depends linearly on the current density in the heavy metal in all films under investigation. $\mu_0 H'_{SL}$ is plotted as measured and not corrected for the planar Hall effect in this figure.

The AHE resistivity ρ_{AHE} as a function of thickness t is shown in Fig. 5.2, on the left axis. ρ_{AHE} is proportional to the magnetic volume, and thus a linear trend can be observed. In addition, the planar Hall effect (PHE) resistivity ρ_{PHE} was measured. ρ_{PHE} also follows a linear trend, however, ρ_{PHE} is two order of magnitude smaller than ρ_{AHE}. The ratio of AHE and PHE is $\xi = \rho_{PHE}/\rho_{AHE} \approx 3.2\,\%$. The right axis of Fig. 5.2 shows the saturation magnetization M_s as a function of thickness. M_s is constant for all samples with $t > 10$ nm. However, the thinnest sample of this series with $t = 10$ nm has a larger M_s. We attribute this increase in M_s to a small shift in composition.

To characterize the SOT in our samples we performed harmonic Hall measurements of the effective magnetic fields, following Hayashi *et al.* [38]. We start by measuring the first and second harmonic voltage responses $V_{1\omega}$ and $V_{2\omega}$ to an AC current with $\omega = 1.2$ kHz

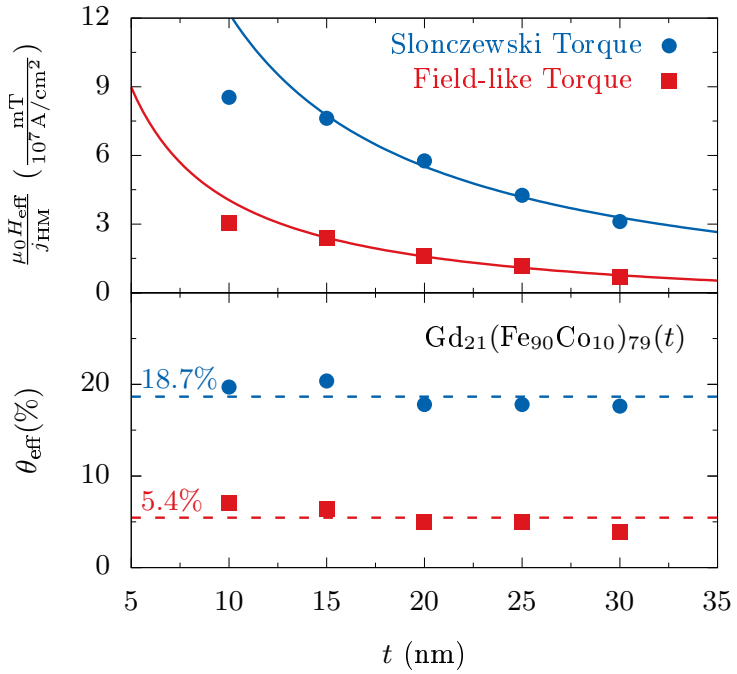

Figure 5.4: The upper panel shows the spin torque efficiency as a function of thickness. We find that both the damping-like (blue dots) and the field-like (red squares) torque efficiency decreases linearly with thickness. The lower panel shows the extracted spin Hall angle $\theta_{\rm SH}$ for the thickness series. Since the thickness t was varied but the HM layers were kept unchanged (and thus the HM/FM interface is constant), the effective spin Hall angle does not depend on the thickness of the FM.

as a function of in-plane magnetic field $B_{x,y}$. To measure the Slonczewski field $H_{\rm SL}$, the in-plane magnetic field B_x is applied along the x-direction, while the in-plane magnetic field B_y is applied along the y-direction to measure the field-like field $H_{\rm FL}$. For all harmonic Hall measurements discussed in the following, the samples were magnetized along the $+z$-direction and thus $m_{\rm tot} > 0$.

A typical harmonic Hall measurement to determine $H_{\rm SL}$ is shown in Fig. 5.3(a) for a $\rm Gd_{21}(Fe_{90}Co_{10})_{79}$ sample with $t = 20\,\rm nm$ and $m_{\rm tot} > 0$. The first harmonic response $R^{1\omega}_{\rm AHE} = V_{1\omega}/I_{\rm FM}$ (blue) follows a quadratic trend as a function of the in-plane magnetic field B_x, while the second harmonic response $R^{2\omega}_{\rm AHE} = V_{2\omega}/I_{\rm FM}$ (red) can be approximated by a linear function of B_x. Here $I_{\rm FM}$ is the current through the $\rm Gd_{21}(Fe_{90}Co_{10})_{79}$.

To compute the effective Slonczewski field from this measurement, the slope of $R^{2\omega}_{\rm AHE}$ is

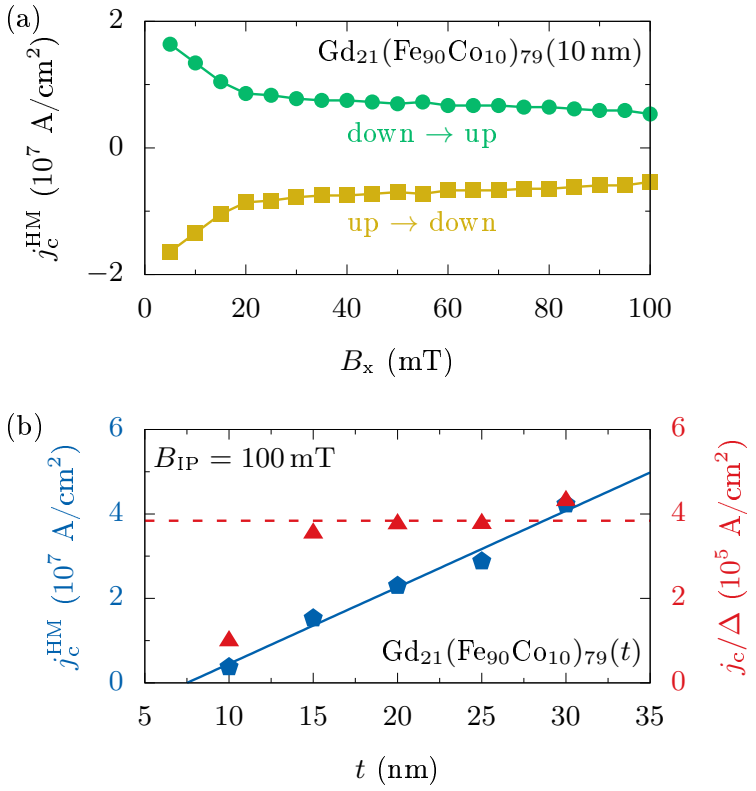

Figure 5.5: Panel (a) shows the switching phase diagram for a $Gd_{21}(Fe_{90}Co_{10})_{79}$ film with thickness $t = 10\,nm$. Panel (b) shows that the critical switching current density depends linearly on the film thickness (blue diamonds, left axis). The ratio j_c/Δ is constant for samples with $t > 10\,nm$ (red triangles, right axis).

divided by the curvature of $R^{1\omega}_{AHE}$ [38]:

$$\mu_0 H'_{SL,FL} = \left(\frac{\partial R^{2\omega}_{AHE}}{\partial B_{x,y}}\right) \times \left(\frac{\partial^2 R^{\omega}_{AHE}}{\partial B^2_{x,y}}\right)^{-1} \tag{5.1}$$

Figure 5.3(b) shows that the effective magnetic field $\mu_0 H'_{SL}$ obtained from this analysis is proportional to the current density in the HM layer in all samples under investigation. This confirms that the effect measured here is indeed caused by SOT, and not by non-linear effects such as heating. In the following, we will refer to the effective field per unit current density through the HM layers as $\zeta_{SL,FL}$.

To account for a mixing of H'_{SL} and H'_{FL} due to the presence of the PHE, the following correction is applied to the data shown in Figure 5.3 [38]:

$$H_{SL,FL} = -2\frac{H'_{SL,FL} + 2\xi H'_{FL,SL}}{1 - 4\xi^2}\,. \tag{5.2}$$

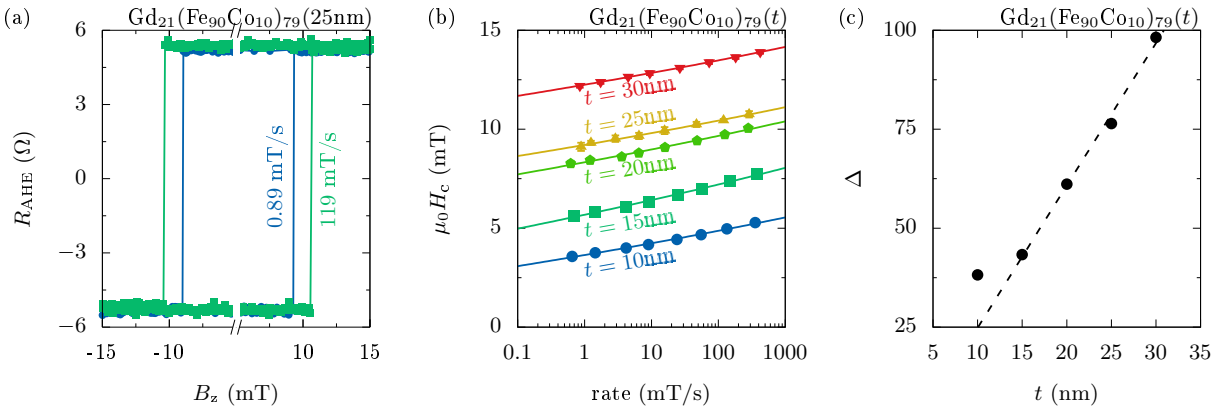

Figure 5.6: Measurement of the thermal stability Δ. Panel (a) shows typical hysteresis loops for the films under investigation. B_z is applied along the easy axis of the magnet. The coercive field $\mu_0 H_C$ is increasing with the sweep rate of the magnetic field due to the thermal nature of the switching events. Panel (b) shows the dependence of $\mu_0 H_C$ on the magnetic field sweep rate. The solid lines are fits to the Chantrell model, which is used to determine the thermal stability factor Δ. The extracted values for Δ are plotted in panel (c) as a function of $Gd_{21}(Fe_{90}Co_{10})_{79}$ thickness.

Here, ξ is the ratio of PHE resistivity and AHE resistivity: $\xi = \rho_{PHE}/\rho_{AHE}$ and the sample is magnetized upwards ($m_{tot} > 0$). The resulting fields $\zeta_{SL,FL}$ are plotted in the upper panel of Fig. 5.4 as a function of $Gd_{21}(Fe_{90}Co_{10})_{79}$ thickness. All samples with $t > 10\,\text{nm}$, follow a $1/t$ dependence. This is consistent with an interfacial torque of the form:

$$\boldsymbol{\tau}_{SOT} = \frac{\hbar}{2e}\frac{j_s}{M_s t}\boldsymbol{m} \times (\boldsymbol{\sigma} \times \boldsymbol{m})\,, \tag{5.3}$$

where e is the electric charge, $\hbar$ Planck's constant and j_s the spin current. The sample with $t = 10\,\text{nm}$ does not follow the trend because M_s is larger (*c. f.* Fig. 5.2) and thus $H_{SL,FL}$ is smaller.

Next we use the results for $\zeta_{SL,FL}$ to calculate the spin-Hall angle θ_{SH} according to:

$$\theta_{SH} = \frac{2|e|}{\hbar} M_s t_{FM} \frac{\mu_0 H_{SL,FL}}{j_{HM}}\,. \tag{5.4}$$

Here losses at the interface were neglected. Figure 5.4 shows that θ_{SH} does not depend on t. This is expected, because the SHA only depends on the choice of SH metal and the interface. Both did not change upon increasing the $Gd_{21}(Fe_{90}Co_{10})_{79}$ thickness. The average value for the SHA is $\theta_{SH} = 18.7\,\%$. This value is well in agreement with literature values in Pt/Co/Ta systems [118].

5.4 Switching Phase Diagram in GdFeCo

In addition to harmonic Hall measurements, we also conducted SOT switching experiments to measure the scaling of critical switching current. To this end, 200 µs long current pulses were applied through the heavy metal layers and the magnetic response was measured by the AHE in the $Gd_{21}(Fe_{90}Co_{10})_{79}$. In order to switch a magnetic film with PMA, an additional magnetic field B_x need to be applied in the x-direction to break the symmetry [68, 31]. First we investigated, how the critical current that is needed to switch the magnet, scales with B_x. A typical switching phase diagram for a $Gd_{21}(Fe_{90}Co_{10})_{79}$ film with $t = 10\,\mathrm{nm}$ is shown in Fig. 5.5(a). As expected, the critical current decreases with increasing B_x. It was further confirmed, that the switching direction is reversed when we change the sign of the in-plane magnetic field [32].

Next we show that the critical current density for SOT-switching j_c at fixed $B_x = 100\,\mathrm{mT}$ scales linearly with t (blue pentagons in Fig. 5.5(b)). This is expected from macro spin simulations if $B_x < \mu_0 H_k$ [59], where H_k is the anisotropy field. The magnitude of j_c is similar to previous results in GdFeCo [96].

5.5 Measurements of the Thermal Stability

Magnetic memory applications require not only low switching current densities but also high thermal stability $\Delta = E_B/k_B T$, where E_B is the activation energy barrier. To investigate the scaling behavior of Δ with t we performed field-switching experiments with an external magnetic field B_z applied along the magnetic easy axis. Field switching is a thermally activated process. Thus, it is expected that the coercive field H_c depends on the rate at which the magnetic field is changed. This is shown in Fig. 5.6(a), where two hysteresis loops, recorded at different sweep rates, are shown. At slow sweeping rates, the switching event occurs at smaller fields, as it is more likely to thermally nucleate a domain, which will then propagate in the magnet.

The dependence of H_c on the sweeping rate has been studied systematically over 3 orders of magnitude on samples with different GdFeCo thickness. The result is shown in Fig. 5.6(b): In a semilogarithmic plot H_c depends approximately linearly on the sweeping rate. Note that each value for H_c is the average value from 20 consecutive field switching measurements. To analyze this data we use a model proposed by El-Hilo *et al.* [25]:

$$H_c = H_k \left(1 - \sqrt{\frac{1}{\Delta} \ln \left[\frac{f_0 H_k}{2\Delta} \frac{1}{r} \right]} \right) . \tag{5.5}$$

Here, H_k is the anisotropy field, Δ is the thermal stability factor, $f_0 = 1 \times 10^{11}\,\mathrm{GHz}$ the attempt frequency and r the sweeping rate. Figure 5.6(b) shows that this model (solid lines) fits the experimental data well. The extracted values for Δ are shown in Fig. 5.6(c). For the extraction we assumed an attempt frequency of $f_0 = 1 \times 10^{10}\,\mathrm{Hz}$.

A linear trend is seen in Fig. 5.6(c) because the thermal stability is proportional to the magnetic volume. The sample with $t = 10\,\mathrm{nm}$ does not follow the trend, which we attribute again to an increase in saturation magnetization.

The switching efficiency for SOT devices is defined as j_c/Δ. In our devices, j_c as well as Δ scale linearly with thickness. Thus, the switching efficiency does not depend on the thickness as shown in Fig. 5.5(b) on the right axis (red triangles).

5.6 Spin-Torques at Different Gd Concentration

All results discussed to far have been obtained on $Gd_x(Fe_{90}Co_{10})_{100-x}$ samples with $x = 21\,\%$. However, it is known that the magnetic properties of TM-RE alloys change drastically with composition [40]. In fact, previous experiments have shown that SOT exhibit a distinctive dependence on the film composition [112, 96, 30, 80]. So far the composition dependence has only been studied in very thin films with $t \leq 5\,\mathrm{nm}$. Further, the effective fields were estimated from domain wall motion experiments [87]. Here we used harmonic Hall measurements to characterize the composition dependence of the effective SOT fields in 30 nm thick $Gd_x(Fe_{90}Co_{10})_{100-x}$ films.

Following eqn. (5.3), we expect the effective magnetic field to diverge at the magnetization compensation point, since M_s will vanish. This trend can clearly be seen in Fig. 5.7, where we plot $\mu_0 H_{SL,FL}/j_{HM}$ vs. the concentration x for the damping-like field as well as for the field-like field.

Next, we calculate θ_{eff}, using the values obtained for $\mu_0 H_{eff}/j_{HM}$. Figure 5.7 shows that θ_{eff} is approximately constant, since only the composition x but not the SH metal or the interfaces were changed. The average value for the SHA is $\theta_{eff} = 18.5\,\%$. This value is well in agreement with the value of θ_{eff} reported in Fig. 5.4.

5.7 Efficient SOT switching in GdFeCo

In conclusion, we showed that the effective magnetic field $H_{SL,FL}$, induced by SOT, scales as $H_{SL,FL} \propto M_s^{-1} t_{FM}^{-1}$ for all samples under investigation in this study. This indicates that the torques are interfacial in nature. θ_{SH} is found to be constant at an average value of $\theta_{SH} = 18\,\%$. We have also shown that $Gd_{21}(Fe_{90}Co_{10})_{79}$ as thick as 30 nm can be switched with SOT currents. j_c, as well as Δ were found to scale linearly with thickness, keeping the switching efficiency j_c/Δ constant. Thus our work, together with torque and thermal stability measurements as a function of thickness, provides a self-consistent picture of how the SOT scales in ferrimagnet/heavy metal heterostructures. The ability to switch large thickness ferrimagnets with high thermal stability might have important implications for future magnetic-memory applications.

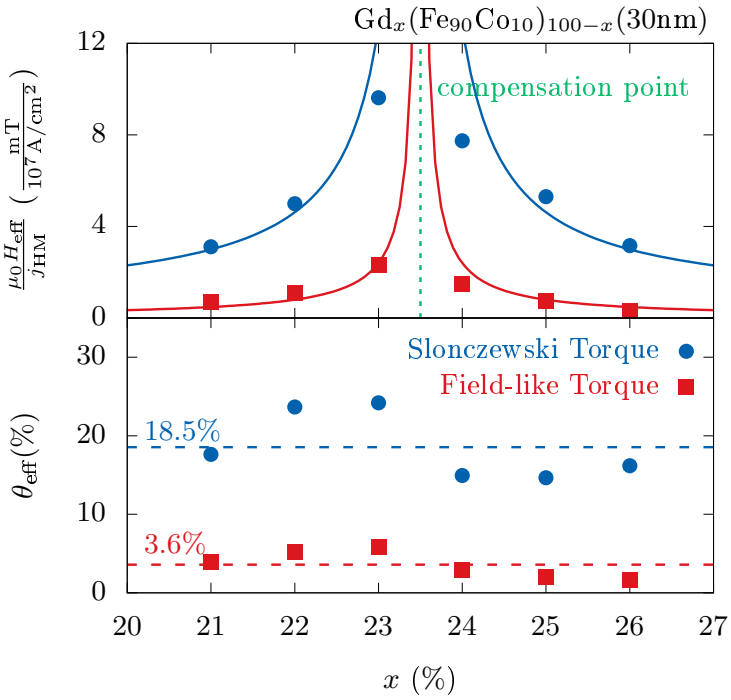

Figure 5.7: Upper panel: The spin torque efficiency as a function of film composition x is shown for the $t = 30\,\text{nm}$ sample. The spin torque efficiency diverges close to the compensation point. Lower panel: The effective spin Hall angle $\theta_{\rm SH}$ is plotted as a function of composition. $\theta_{\rm SH}$ shows no distinct dependence on the composition x, since the HM/FM interface is unaltered.

Chapter 6

Spin-Orbit Torque in Topological Insulators

Harmonic measurements of the longitudinal and transverse voltages in Bi-Sb\Co bilayers are presented. A large second harmonic voltage signal due to the ordinary Nernst effect is observed. In experiments where a magnetic field is rotated in the film plane, the ordinary Nernst effect shows the same angular dependence in the transverse voltage as the damping-like spin-orbit torque and in the longitudinal voltage as the unidirectional spin-Hall magnetoresistance respectively. Therefore, the ordinary Nernst effect can be a spurious signal in spin-orbit torque measurements, leading to an overestimation of the spin-Hall angle in topological insulators or semimetals.

6.1 Spin Current Generation at Topological Insulators Interfaces

In metal-based spintronics, heavy metals such as platinum, tantalum or tungsten are used to convert charge currents into spin-currents via the spin-Hall or Rashba-Edelstein effect [79, 31, 67, 65]. These spin currents can be used to manipulate the magnetization of a magnet, which has useful application in memory technology [61, 21].

One way to quantify the spin-to-charge conversion efficiency is to measure the the spin-Hall angle θ_{SH}. While the reported magnitude of the spin-Hall angle varies somewhat in the literature, it is generally agreed that the spin-Hall angle in heavy metals is of the order of 10% [91]. To make a significant impact in memory applications, a larger spin-to-charge conversion efficiency, i.e., a larger spin Hall angle is desired [2, 24]. In this regard, topological insulators gained immense interest recently due to the unique spin-momentum locking they offer, which could lead to significantly higher spin to charge conversion efficiency [42]. Indeed, various research groups have reported the observation of large spin Hall angles compared to those observed in heavy metal layers using various characterization methods, such as harmonic Hall voltage measurements [28, 22, 63], spin pumping [23, 100, 47, 114, 34, 92,

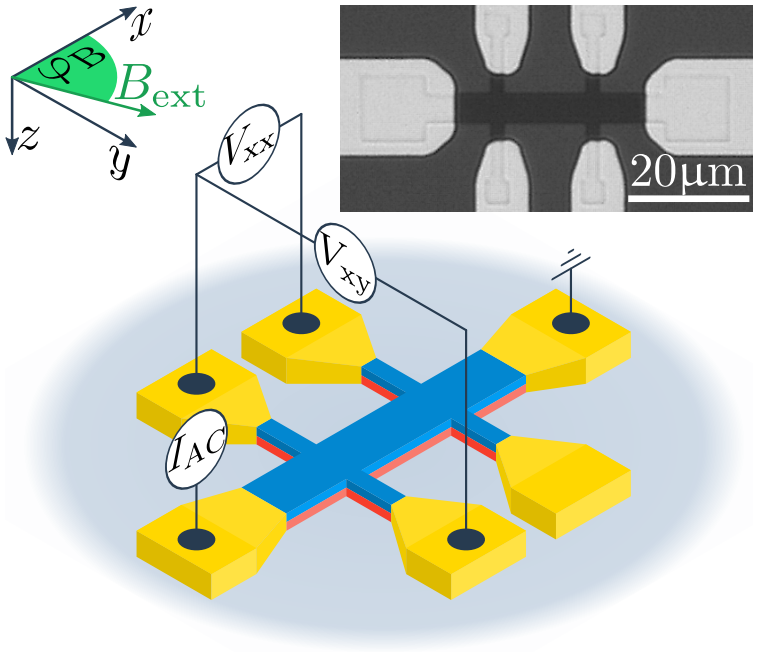

Figure 6.1: A double Hall-bar structure is used to measure transverse (V_{xy}) and longitudinal (V_{xx}) voltages on the Bi-Sb bilayer samples considered in this work. The magnetic field is applied in the film plane at an angle φ with respect to the current direction. The inset shows a micro-graph of an actual double Hall-bar device. The width of the Hall bar is 6 µm.

83], spin-Seebeck effect measurements [75], spin-polarized tunneling studies [66, 58], domain wall motion experiments [54, 36] and spin-torque ferromagnetic resonance [117, 99, 55, 116, 74].

In addition, it has been reported that the unidirectional spin-Hall magneto-resistance (USMR) is orders of magnitudes larger in topological insulator\heavy metal bilayer films than in conventional heavy metal\ferromagnet bilayers [122, 44, 72, 39]. Since the unidirectional magneto-resistance is asymmetric in the current direction as well as the magnetic field direction, harmonic voltage measurements are often used to quantify this phenomenon [6].

6.2 The Ordinary Nernst Effect in Topological Insulators

While these aforementioned reports have given credence to the promise of using topological insulator materials for high efficiency electronics applications, there are also recent reports that indicate how the extracted spin Hall angles could be impacted by spurious signals. For example, Yasuda *et al.* [121] have discussed how asymmetric magnon scattering could influence the magnitude of the spin Hall angle. Similarly, it has been observed recently that

the Seebeck effect can be a spurious signal in spin-pumping experiments [115]. From both the points of view of understanding the underlying physics and its ultimate adoption for an application, it is important to identify the sources of spurious signals in the quantification of the spin Hall angle. In this work, we show that there is an additional source, stemming from the ordinary Nernst effect (ONE) [64, 125], that could significantly influence the observations made in harmonic Hall measurements, especially for semiconducting spin Hall materials such as the topological insulators.

Notably, ONE refers to the generation of a voltage, when both a temperature gradient and a magnetic field are present [1]. The thermal voltage scales linearly with the external magnetic field and has not been taken into account in previous SOT experiments. Therefore the presence of the ONE in topological insulators at room temperature might give an explanation for the giant spin Hall angles reported recently. Further the ONE can contribute to the longitudinal voltage signal in USMR-type measurements.

Two control experiments will be discussed in the following to separate thermal effects from SOT and USMR. First, we will compare the harmonic voltage response in Bi-Sb\Co samples to that in Bi-Sb\Al samples. While in Bi-Sb\Co, voltages can arise due to magneto-transport effects, the effects in Bi-Sb\Al will be purely thermal. Secondly we will explore the magnetic field dependence of the voltage response. While spin-orbit torque effects are expected to be suppressed by large magnetic fields, the thermal voltage due to the ONE increases linearly with magnetic field.

6.3 Epitaxial growth of Bi-Sb

The samples discussed in this work are $Bi_{0.74}Sb_{0.26}(4)\backslash Co(4)$, $Bi_{0.96}Sb_{0.04}(10)\backslash Al(5)$ and Pt(5)\Py(5) (thickness in nm). We refer to these samples as Bi-Sb\Co, Bi-Sb\Al and Pt\Py respectively. All samples are capped with 2.5 nm Si_3N_4. The Bi-Sb is grown epitaxially on high resistivity ($> 20\,k\Omega\,cm$) Si(111) substrate by molecular beam epitaxy. Bulk samples of both $Bi_{0.74}Sb_{0.26}$ and $Bi_{0.96}Sb_{0.04}$ are semi-metals [62, 46]. It has been reported that a band gap opens up in thin films of $Bi_{0.74}Sb_{0.26}$ due to quantum confinement effects. Therefore $Bi_{0.74}Sb_{0.26}$ films may show topological insulating behavior [113].

Co is deposited with e-beam evaporation onto the Bi-Sb ex-situ and the magnetic easy axis is in the film plane. Al, Pt and Py are grown by magnetron sputtering. After growth, optical lithography and Ar-ion milling are used to pattern Hall bar devices, as shown in the inset of Fig. 6.1. The width of the Hall bar is 6 µm and the distance between 2 Hall crosses is 20 µm. The current is applied along the x-direction while the longitudinal and transverse voltages (V_{xx} and V_{xy}) are measured. An external magnetic field B_{ext} is applied in the film plane at an angle φ_B with respect to the current direction. The samples have the following resitivities: $\rho_{\text{Bi-Sb\backslash Co}} = 127\,\mu\Omega\,cm$, $\rho_{\text{Bi-Sb\backslash Al}} = 419\,\mu\Omega\,cm$ and $\rho_{\text{Pt\backslash Py}} = 27\,\mu\Omega\,cm$.

In all experiments reported here the magnetic field is sufficient to fully saturate the magnet along the field-direction for all angles φ_B. Further, all experiments were performed at room temperature and at constant Joule-heating power of $P_{\text{heat}} = I^2R = 0.18\,mW$.

6.4 Harmonic Hall Measurements of Thermal Effects in Bi-Sb

For harmonic measurements presented in this work, an ac current $I = I_0 \cdot \sin(\omega t)$ with $\omega/2\pi = 1.5\,\mathrm{kHz}$ is applied. If SOT is present, the ac current can induce quasi static magnetization oscillations and thus periodic changes of the resistance and Hall resistance. Therefore, in addition to the first harmonic voltage response V^{ω}, a second harmonic voltage $V^{2\omega}$ will be induced at twice the excitation frequency [4].

Further, the ac current induces a periodic temperature gradient. Since Joule heating is quadratic in the current, a second harmonic voltage response can also be induced by thermal effects such as the ordinary Nernst effect [17, 64], the anomalous Nernst effect [20, 4] or the longitudinal spin-Seebeck effect [98].

The first harmonic Hall voltage can be written as:

$$V_{1\omega}^{xy} = V_{\mathrm{PHE}} \cdot \sin(2\varphi_B),$$
$$V_{1\omega}^{xx} = V_{\mathrm{AMR}} \cdot \cos(2\varphi_B).$$

Here, φ_B is the angle between the current and the external magnetic field B_{ext} in the film plane (cf. Fig. 6.1), V_{PHE} is the planar Hall effect amplitude and V_{AMR} is the amplitude of the anisotropic magneto-resistance. The second harmonic voltage is written as [4]:

$$\begin{aligned} V_{xy}^{2\omega} =& \left(\frac{V_{\mathrm{AHE}}}{2} \frac{\Delta B_{\mathrm{DL}}}{B_{\mathrm{ext}} + \mu_0 M_{\mathrm{eff}}} + A\alpha\nabla T + N\alpha B_{\mathrm{ext}} \nabla T \right) \cos(\varphi_{\mathrm{B}}) \\ &+ \left(V_{\mathrm{PHE}} \frac{\Delta B_{\mathrm{FL}}}{B_{\mathrm{ext}}} \right) \cos(2\varphi_{\mathrm{B}}) \cos(\varphi_{\mathrm{B}}) \,, \end{aligned} \tag{6.1}$$

$$\begin{aligned} V_{xx}^{2\omega} =& \left(V_{\mathrm{USMR}} + A\beta\nabla T + N\beta B_{\mathrm{ext}} \nabla T \right) \sin(\varphi_{\mathrm{B}}) \\ &+ \left(V_{\mathrm{AMR}} \frac{\Delta B_{\mathrm{FL}}}{B_{\mathrm{ext}}} \right) \sin(2\varphi_{\mathrm{B}}) \cos(\varphi_{\mathrm{B}}) \,, \end{aligned} \tag{6.2}$$

where V_{AHE} is the anomalous Hall effect voltage, ΔB_{DL} is the effective field due to the damping like torque, $\mu_0 M_{\mathrm{eff}}$ is the effective magnetization, A is the coefficient for the ANE/ SSE, α and β are geometrical factors, ΔT is the temperature gradient, N is the ordinary Nernst coefficient, ΔB_{DL} is the effective field due to field-like torque and V_{USMR} is the amplitude of the unidirectional spin-Hall magneto-resistance.

The field-like SOT can be extracted from the φ_{B} dependence of the second Harmonic voltage signal. However, it is important to consider the magnetic field dependence in addition to the φ_{B}-dependence for the extraction of the damping-like SOT, as well as the USMR, to distinguish magneto-thermal effects from SOT.

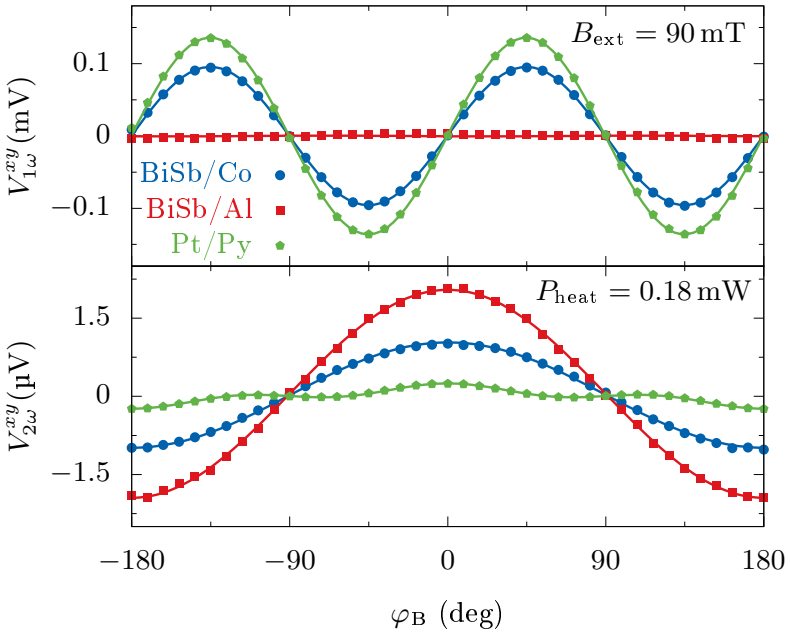

Figure 6.2: Upper panel: The planar Hall effect is only observed in the samples with magnetic layers (Bi-Sb\Co and Pt\Py). Here, φ_{B} is the angle between the current direction and B_{ext} in the film plane. Lower panel: $V_{2\omega}$ shows a $\cos(\varphi_{\text{B}})$ dependence in the samples with Bi-Sb, due to the ordinary Nernst effect. In the sample Pt\Py, spin-orbit torque and anomalous Nernst effect are present. The solid lines are fits to eq.(6.1).

6.5 Angular Dependence of the Harmonic Voltage

We start by discussing the angular dependence of the transverse harmonic voltages. The top panel in Fig. 6.2 shows $V_{xy}^{1\omega}$ as a function of φ_{B}. In the samples Bi-Sb\Co and Pt\Py, a $\sin(2\varphi_{\text{B}})$-dependence can be seen. This is due to the presence of the PHE in the Co and Py layers respectively. $V_{xy}^{1\omega}$ does not depend on B_{ext} in Bi-Sb\Al, due to the absence of a magnetic layer.

The second harmonic Hall voltage $V_{xy}^{2\omega}$ is shown in the bottom panel of Fig. 6.2. In all 3 samples under consideration, $V_{xy}^{2\omega}$ vs. φ_{B} can be well fitted by Eq. (6.1) (solid lines). In the Pt\Py sample contributions from the field-like torque are clearly visible. On the other hand, samples Bi-Sb\Co and Bi-Sb\Al do not show the characteristic $\cos(2\varphi_{\text{B}})\cos(\varphi_{\text{B}})$-dependence. Since no magnet is present in the sample Bi-Sb\Al, the large second harmonic voltage is attributed to the ONE.

The fact that no field-like torque is observed in the sample Bi-Sb\Co, as well as the fact that voltage signals in Bi-Sb\Al and Bi-Sb\Co are comparable gives rise to the suspicion that the signal in the sample Bi-Sb\Co might be dominated by the ONE. To unambiguously distinguish the ONE from SOT, the B_{ext}-dependence will have to be considered, which we will discuss after the following discussion on USMR measurements.

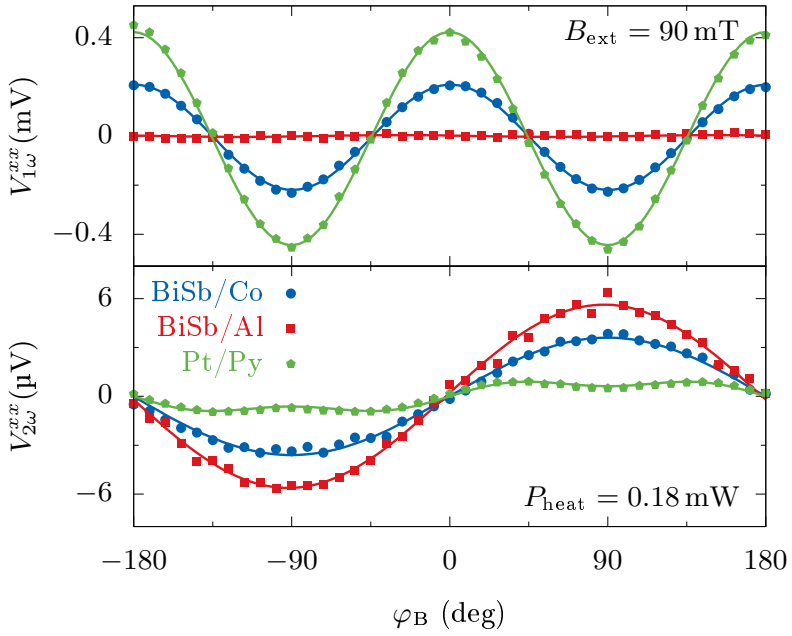

Figure 6.3: Upper panel: $V_{1\omega}^{xx}$ as a function of φ_{B}. A constant offset was removed for easy comparison. The anisotropic magneto-resistance is observed only in the magnetic samples, Bi-Sb\Co and Pt\Py. Lower panel: $V_{2\omega}^{xx}$ in Bi-Sb\Co and Bi-Sb\Al shows a $\sin(\varphi)$ dependence. This is expected from the ordinary Nernst effect. In the sample Pt\Py contributions from spin-orbit torque, anomalous Nernst effect and the unidirectional spin-Hall magneto-resistance are observed. The solid lines are fits to Eq.(6.2).

In addition to the angular dependence of V_{xy}, the longitudinal voltage V_{xx} was measured (Fig. 6.3). Again, a signal from the anisotropic magneto-resistance (AMR) is only observed in the samples with a magnetic layer (top panel), while all samples show an angular dependence of $V_{2\omega}^{xx}$ that can be well described with Eq. (6.2) (bottom panel). In the Pt\Py reference sample, a clear signature from field-like SOT ($\propto \sin(2\varphi_{\text{B}})\cos(\varphi_{\text{B}})$) can be observed while the USMR ($\propto \sin(\varphi_{\text{B}})$) is small. The sample Bi-Sb\Al shows a $\sin(\varphi)$-dependence due to the ONE. The absence of field-like torque in Bi-Sb\Co, as well as a signal amplitude comparable to the signal in Bi-Sb\Al raises the suspicion that the signal in Bi-Sb\Co is dominated by the ONE and not a large USMR.

6.6 Magnetic Field Scaling of the Ordinary Nernst Effect in Bi-Sb

To determine the origin of the large voltages observed in Bi-Sb\Co, we repeat the measurements shown in Fig. 6.2 and Fig. 6.3 for different values of B_{ext}. Figure 6.4 shows the $\cos(\varphi_B)$

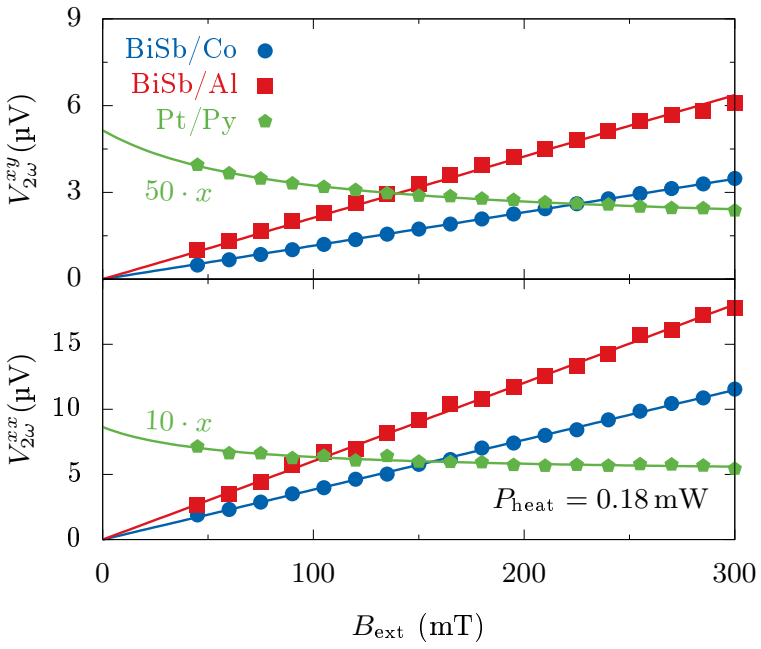

Figure 6.4: The magnetic field dependence of the second harmonic voltage. In Bi-Sb\Co and Bi-Sb\Al a linear increase in voltage can be observed, as expected from the ordinary Nernst effect. In Pt\Py on the other hand the harmonic voltage is decreasing as expected from damping-like spin-orbit torque and unidirectional spin-Hall magneto-resistance respectively. Note that the voltage in Pt\Py has been enhances for visual clarity.

contribution to $V_{2\omega}^{xy}$ and the $\sin(\varphi_B)$ contribution to $V_{2\omega}^{xx}$ respectively. In the reference sample Pt\Py, $V_{2\omega}^{xy}$ decreases with increasing B_{ext}. This is expected, because large magnetic fields suppress the quasi-static magnetization oscillations induced by SOT (cf. Eq. (6.1)). On the other hand, $V_{2\omega}^{xy}$ increases linearly with B_{ext} in the samples Bi-Sb\Co and Bi-Sb\Al. This is clear evidence for the presence of ONE. Note that $V_{2\omega}^{xy}$ is ≈ 50 times larger in the samples with Bi-Sb.

Similarly, a clear presence for the USMR is seen only in the sample Pt\Py (Fig. 6.4, bottom panel): $V_{2\omega}^{xx}$ decreases with increasing B_{ext}, in accordance with recent reports by Avci *et al.* [5] The samples Bi-Sb\Al and Bi-Sb\Co show a linear dependence on B_{ext}, as expected from the ONE. The slope of $V_{2\omega}^{xx}$ vs B_{ext} in Bi-Sb\Co is $V_{2\omega}^{xy}/B_{\text{ext}} = (0.011 \pm 0.006)\,\text{V}\,\text{mT}^{-1}$ and $V_{2\omega}^{xx}/B_{\text{ext}} = (0.038 \pm 0.003)\,\text{V}\,\text{mT}^{-1}$ respectively. The different values obtained for the longitudinal and transverse voltages are explained by the geometric factors α and β in eq. 6.1 and Eq. 6.2. The ratio is $V_{2\omega}^{xx}/V_{2\omega}^{xy} = \beta/\alpha = l/w = 3.3$, where l is the distance between two Hall crosses and w the width of the Hall bar. This geometrical scaling is a strong indicator that $V_{2\omega}^{xy}$ and $V_{2\omega}^{xx}$ have the same physical origin. Note that USMR and SOT are distinctly different phenomena and it can not be expected that they would scale with the device geometry.

Next we will calculate the ONE coefficient N and show that N is equal in samples Bi-Sb\Co and Bi-Sb\Al. To this end we estimate the temperature gradient using the 1D heat equation $T''(z) = \dot{q}_i/\kappa$, where $T(z)$ is the temperature, $\dot{q}_i$ is the volumetric power density and κ the thermal conductivity. The boundary conditions at the interfaces are:

$$T_i = T_{i+1} \ , \quad \kappa_i \frac{\partial T_i}{\partial z} = \kappa_{i+1} \frac{\partial T_{i+1}}{\partial z}$$

We assume no heat conduction at the surface of the sample and a fixed temperature at the backside of the substrate. The following values for the thermal conductivity have been used: $\kappa_{\text{Bi-Sb}} = 6.8\,\text{W}\,\text{m}^{-1}\,\text{K}^{-1}$ [123], $\kappa_{\text{Co}} = 98\,\text{W}\,\text{m}^{-1}\,\text{K}^{-1}$ [110] and $\kappa_{\text{Al}} = 238\,\text{W}\,\text{m}^{-1}\,\text{K}^{-1}$ [88]. At a heating power of $P = 180\,\mu\text{W}$, the temperature gradient is $\Delta T_{\text{Bi-Sb\Co}} = 6.6\,\text{mK}$ and $\Delta T_{\text{Bi-Sb\Al}} = 18\,\text{mK}$. Using these values, we find $N = 3 \times 10^{-6}\,\text{V}\,\text{T}^{-1}\,\text{K}^{-1}$ in Bi-Sb\Co and $N = 2.6 \times 10^{-6}\,\text{V}\,\text{T}^{-1}\,\text{K}^{-1}$ in Bi-Sb\Al. These values are well in agreement and confirm the same origin of $V_{2\omega}$ in the samples Bi-Sb\Co and Bi-Sb\Al, namely the ordinary Nernst effect. Further, N is of the same order of magnitude in other semi-conducting materials [10].

6.7 Power Scaling of the Ordinary Nerst Effect

To explore how the ordinary Nernst effect as well as spin-orbit torque scale with the heating power, the measurement presented in Fig. 6.4 was repeated at different different current densities. The result is shown in Fig. 6.5. Since $V_{2\omega}$ scales linearly with B_{ext} in the samples Bi-Sb\Co and Bi-Sb\Al, the slope $V_{2\omega}/B_{\text{ext}}$ is shown as a function of the heating power P_{heat}. While $V_{2\omega}$ clearly increases with increasing heating power small deviations from a linear dependence can be observed. This non-linearity is attributed to changes in the thermal conductivity and changes in the samples resistance with temperature.

In the reference sample Pt\Py, $V_{2\omega}$ is not a linear function of B_{ext} as expected from spin-orbit torque. Instead, the second harmonic voltage scales as $V_{2\omega} \propto (1/B_{\text{ext}} + \mu_0 M_{\text{eff}})$. For this end, we fit an inverse function to the $V_{2\omega}$ vs. B_{ext} data points and plot $V_{2\omega} \cdot B_{\text{ext}}$ as a function of P_{heat}. As expected, a linear function is observed. This is well in agreement with that fact that thermal effect in the Pt\Py samples are small due to the metallic nature of the reference layers.

6.8 Summary and Conclusions

In summary, harmonic measurements of the longitudinal and transverse voltages in Bi-Sb\Co films are presented. We find strong evidence that the second harmonic voltage in our samples is dominated by contributions from the ordinary Nernst effect: The longitudinal and transverse voltages scale with the device geometry. Further, we show that the ordinary Nernst effect has the same amplitude in Bi-Sb\Al samples where magneto-transport effects are absent. In fact, we find that the voltages from the ordinary Nernst effect is an order of magnitude larger than voltages expected from SOT or USMR, which makes the detection

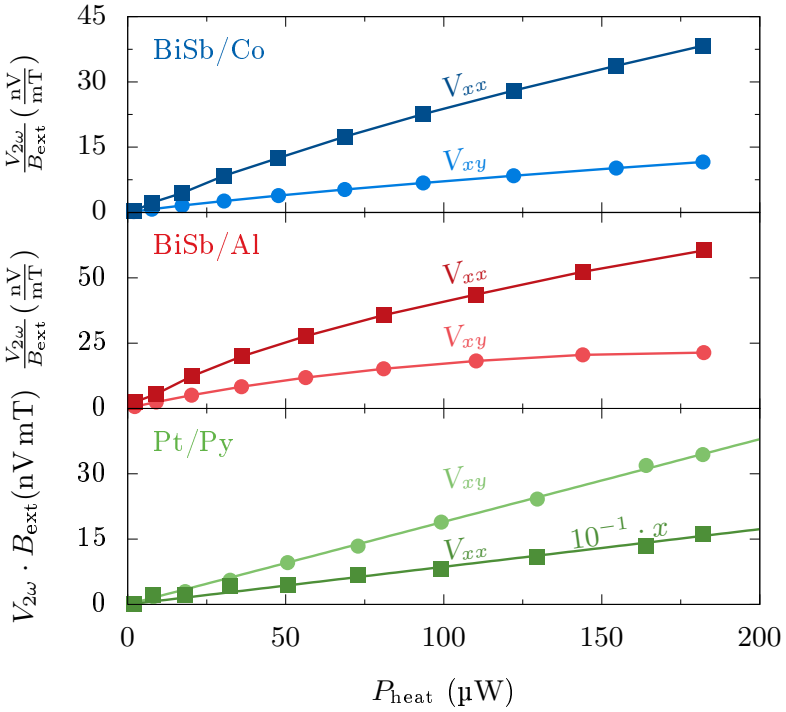

Figure 6.5: The power dependence of the second harmonic voltage. Since $V_{2\omega}$ scales linearly with B_{ext} in the samples Bi-Sb\Co and Bi-Sb\Al, the slope is plotted for these samples. In the reference sample Pt\Py, the amplitude of the inverse function $\frac{V_{\mathrm{AHE}}}{2}\frac{\Delta B_{\mathrm{DL}}}{B_{\mathrm{ext}}+\mu_0 M_{\mathrm{eff}}}$ is shown. The voltage in the reference sample scales linearly with the power. However, in the Bi-Sb samples deviation from the linear power dependence are observed at large powers.

of pure spin related effects highly challenging. It has further been reported that the surface states of a TI are destroyed by a ferromagnet at the interface due to direct exchange [92, 83]. The low thermal conductivity of Bi-Sb due to it's semiconducting nature is predominantly responsible for the large ONE related voltages observed in our experiments. Given that the symmetry of the ONE related voltages are the same as those originating from spin orbit torque, it is critical to measure the harmonic voltages as a function of the external magnetic field amplitude to distinguish different contributions such as ANE, ONE and SOT/USMR.

Chapter 7

MRAM Performance Under Mechanical Strain

In this chapter the effect of the mechanical stress on the performance of magnetic tunnel junctions (MTJ) with perpendicular magnetic anisotropy is investigated. We developed a 4-point bending setup, that allows us to apply a constant stress over a large substrate area with access to electrical measurements and external magnetic field. This setup enables us to measure key device performance parameters, such as tunnel magnetoresistance (TMR), switching current ($I_c^{50\%}$) and thermal stability (Δ), as a function of applied stress. We find that variations in these parameters are negligible: less than 2 % over the entire measured range between the zero stress condition and the maximum stress at the point of wafer breakage.

7.1 Strain in MTJ with Perpendicular Magnetic Anisotropy

Recently, several companies have announced integration of embedded Magnetic Random Access Memory (MRAM) with existing CMOS logic [51, 102, 105]. Spin transfer torque (STT) MRAM is a non-volatile memory technology that offers high speeds, low energy consumption and high endurance [2, 53]. The fundamental building block of STT-MRAM is a magnetic tunnel junction (MTJ), which consists of two ferromagnetic layers separated by a tunneling barrier. Readout of the MRAM bit is enabled by the tunnel magnetoresistance (TMR) of the MTJ [50, 81], while write operations are based on STT switching [11, 103].

An important design parameter for MRAM is the strain applied to the ferromagnetic layers of the MTJ. Strain can impact the magnetic and electronic properties of a magnet as well as the quantum transport across the tunneling barrier. The TMR of a MTJ with in-plane anisotropy changes significantly under application of stress [70]. In fact, Loong et al. have seen an enhancement of the TMR by 68 % [71] under the application of inhomogeneous

strain. Furthermore, strain and pressure sensors based on the magneto elastic coupling of CoFe have been demonstrated [69, 108, 109, 76, 86, 19].

Previous work on the strain dependence of MTJs has focused on devices with in-plane magnetic anisotropy. State of the art memory elements, however, utilize MTJs having thinner free layers with out of plane anisotropy due to better scalability and faster switching times [107, 119, 84, 97].

In this work we characterize MTJs with out of plane magnetic anisotropy under systematic application of strain. In addition to the TMR, we also study the strain dependence of other important performance parameters, such as the critical write current $I_c^{50\%}$ and the thermal stability factor Δ. To apply the strain in a systematic way, we have designed an integrated 4-point bending setup [9] with a magnetic probe station. This 4-point bending setup allows us to apply constant strain over large substrate areas while magnetotransport measurements are carried out.

We present the surprising result that transport in our MTJ devices with perpendicular magnetic anisotropy is very robust to mechanical stress. Our findings show that while the TMR and the thermal stability factor Δ are independent of external strain (within the accuracy of the measurement), we observe a small decrease of the coercive field $\mu_0 H_c$ and the switching current $I_c^{50\%}$ with increasing strain.

7.2 4-point Bending Setup for Application of Constant Strain

Figure 7.1 shows a sketch of our 4-point bending setup. Two ceramic rods support the wafer from the top while a force is applied from the bottom to bend the wafer. The strain ϵ in the center region between the two supporting rods is constant. This strain is related to the bending curvature κ as $\epsilon = \kappa \cdot y$, where y is the distance to the neutral plane, i.e the wafer thickness divided by 2.

The MTJs under investigation in this study are deposited on top of a 775 µm thick silicon wafer with 100 nm thermal oxide. The MTJ stack consists of a synthetic antiferromagnet, i.e. layered ferromagnets with antiferromagnetic coupling, serving as a reference (pinned) layer, and a CoFeB-based free layer separated by a MgO tunnel barrier. Both layers have perpendicular magnetic anisotropy. Tunnel junction devices are patterned, using conventional ion milling technique, into circles with diameter d from 40 nm to 80 nm. All measurements of the electrical resistance R are performed in a two terminal geometry with the contact resistance taken into account.

To protect our samples from damage due to uncontrolled shattering we first examine the maximum strain that can be applied to the wafer before a catastrophic breakage event occurs. We find that the average breaking point of the silicon wafers used for this study is at $\epsilon \approx 0.1\,\%$. Assuming the value of $Y = 150\,\mathrm{GPa}$ for the Young's modulus of silicon, this corresponds to a stress level of $\sigma = 150\,\mathrm{MPa}$. To prevent wafer breakage, the maximum

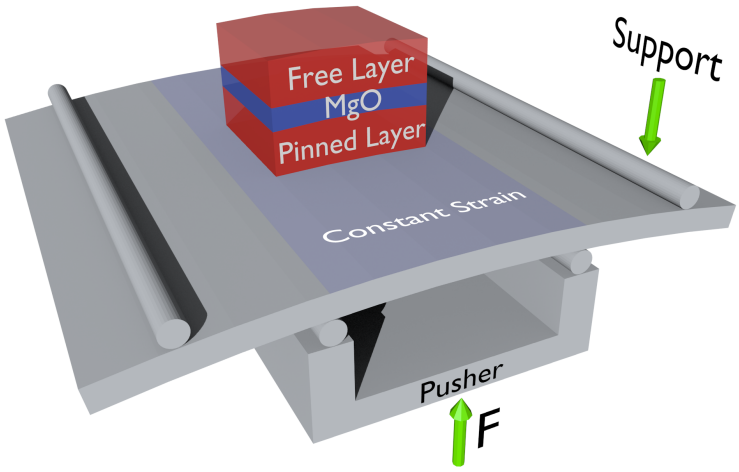

Figure 7.1: Schematics of the 4-point bending setup. The wafer is pushed up by a force F in the center while two supporting pins hold the position fixed at the outside edges. The mechanical stress in the central region (light gray) is constant. The magnetic tunneljunctions under test have perpendicular magnetic anisotropy.

strain applied in this study is thus limited to 0.06 %.

7.3 Stress Dependence of the Tunnel Magneto Resistance

We first measure RH-minor loops by sweeping an external magnetic field along the easy axis of the free layer. Figure 7.2(a) shows two switching events and clearly distinguishable high and low resistance states. The coercive field of the free layer $\mu_0 H_c$ as well as the TMR ratio are extracted from this measurement. A summary of the normalized TMR ratio and $\mu_0 H_c$ as a function of strain is shown on Fig. 7.2(b). Each value reflects the mean of 46 RH-loops on 63 different devices. The obtained values for the TMR ratio are remarkably constant over the whole range of strain, with variations less than 1 %. The coercive field decreases slightly with increasing strain. This decrease is attributed to the magnetoelastic coupling of the free layer.

7.4 Spin Torque Switching

Next, the critical current for spin-transfer torque switching is considered. We define the critical current $I_c^{50\%}$ as the current with 50% switching probability. Experimentally, $I_c^{50\%}$

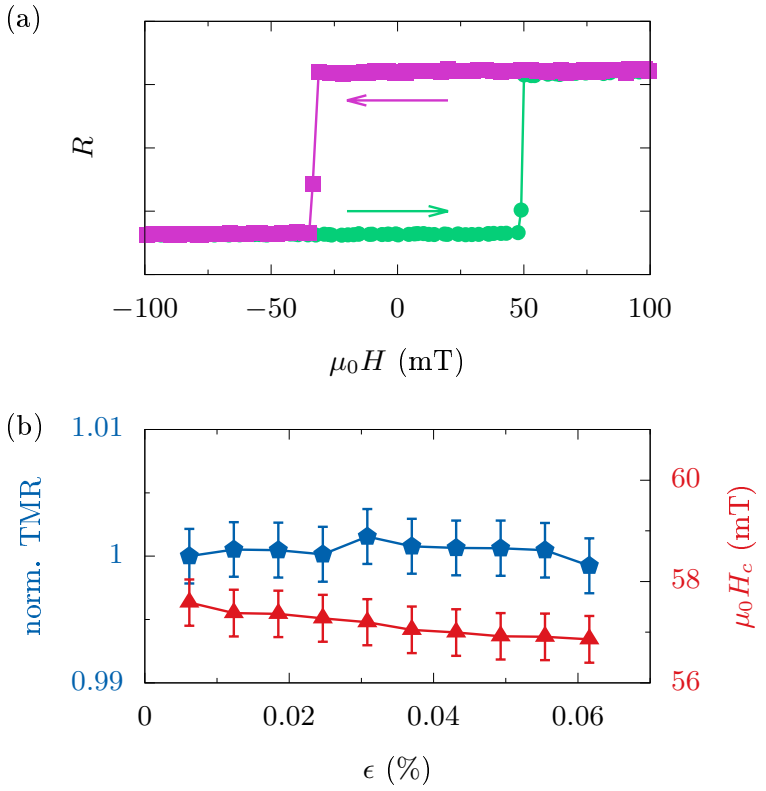

Figure 7.2: (a) RH minor loop for a typical magnetic tunnel junction (MTJ) under test. Arrows indicate the sweep direction. (b) Tunnel magnetoresistance TMR (left) and coercive field $\mu_0 H_c$ (right) as a function of strain ϵ. The TMR is constant with variations less than 1%. The coercive field decreases by less than 1 mT over the full measurement range.

is derived from write error rate (WER) measurements. For this end, we apply a series of current pulses and measure the switching probability.

Figure 7.3(a) shows $I_{50\%}$ as a function of the current pulse width t_{PW}. At long current pulses ($t_{\mathrm{PW}} > 500\,\mathrm{ns}$), the switching process is thermally activated (cyan region) and $I_{50\%}$ depends logarithmically on t_{PW} [9]:

$$I_c = I_{c0}\left[1 - \sqrt{\frac{1}{\Delta}\log\frac{t_{\mathrm{PW}}}{\tau_0}}\right].$$

Here Δ is the thermal stability, τ_0 is the intrinsic attempt time and I_{c0} is the intrinsic switching current. The solid lines in Fig. 7.3(a) are fits to the model above. For short pulses with $t_{\mathrm{PW}} < 500\,\mathrm{ns}$, precessional switching is observed, where $I_c \propto 1/t_{\mathrm{PW}}$ [119]. The dotted line in the yellow regime in Fig. 7.3(a) indicates this inverse trend.

The critical current at $t_{\mathrm{PW}} = 100\,\mathrm{ns}$, $I_{50\%}^{100\,\mathrm{ns}}$, is shown as a function of strain in Fig. 7.3(b). As in Fig 7.2(b) we show the average value for 63 tested devices. For both switching direc-

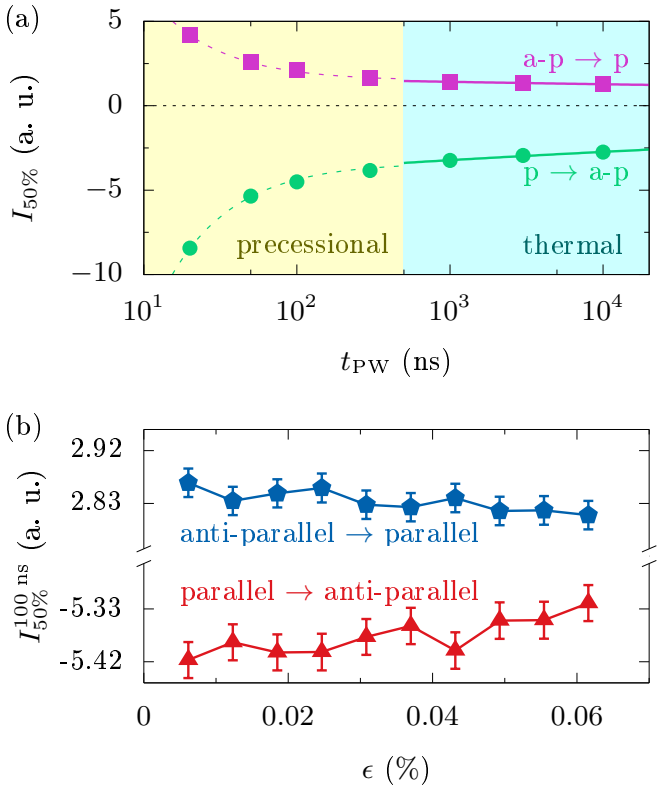

Figure 7.3: (a) Measurement of the critical switching current $I_{50\%}$ as a function of pulse width t_{PW}. $I_{50\%}$ is defined as the current where the switching probability is 50 %. Solid lines indicate fits to a thermal activation model. At short pulses with $t_{\mathrm{PW}} < 500\,\mathrm{ns}$, precessional switching is observed (dotted line). (b) shows the switching current at 100 ns pulse width $I_{50\%}^{100\,\mathrm{ns}}$ as a function of strain. For both switching directions, $I_{50\%}^{100\,\mathrm{ns}}$ is reduced at higher strain.

tions, $I_{50\%}^{100\,\mathrm{ns}}$ decreases with increasing strain. At 0.06 % strain, $I_{50\%}^{100\,\mathrm{ns}}$ is reduced by $\approx 1.5\,\%$. The decrease in $I_{50\%}^{100\,\mathrm{ns}}$ is similar to the reduction in $\mu_0 H_c$ with increasing strain.

7.5 Thermal Stability Characterization

The thermal stability Δ is derived from deep WER measurements. The switching probability P_{SW} is plotted as a function of current pulse amplitude I_{Pulse} in Fig. 7.4(a). We chose a pulse length of $t_{\mathrm{PW}} = 100\,\mathrm{ns}$ and measured deep error rates down to $P_{\mathrm{SW}} = 10^{-6}$. The thermal stability Δ is calculated according to [16]:

$$\Delta = -\log(P_{\mathrm{SW}}^0) + \log(t_{\mathrm{PW}})\,,$$

where P_{SW}^0 is the extrapolated switching probability at $I_{\mathrm{Pulse}} = 0$.

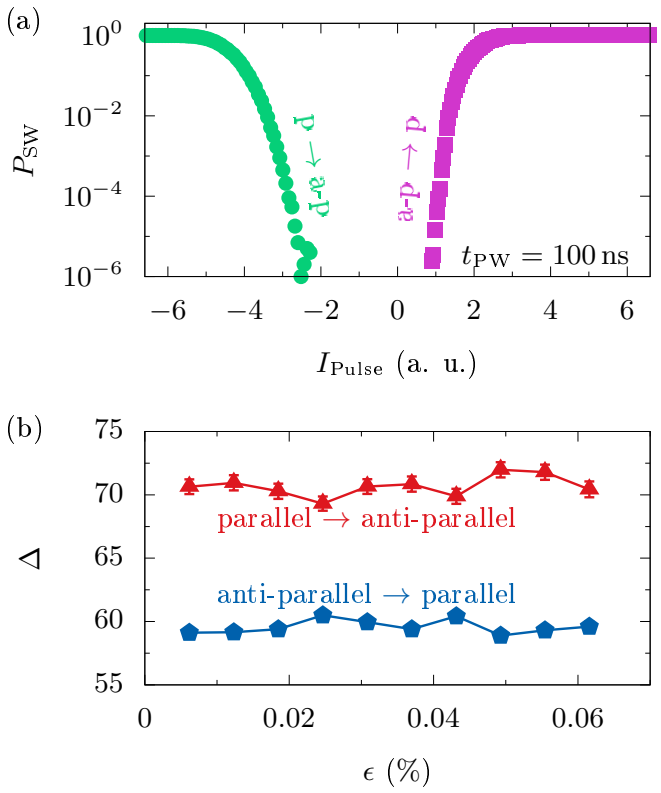

Figure 7.4: (a) For write error rate (WER) testing, the switching probability is measured as a function of pulse amplitude. The pulse length is $t_{PW} = 100\,ns$. (b) Thermal stability factor Δ, extracted from WER measurements, as a function of strain. The thermal stability does not show any variation as a function of strain within the measurement accuracy.

Figure 7.4(b) shows Δ, averaged for 63 devices, as a function of strain. Δ is constant for all strain values tested. It should be noted that the noise in this measurement is on the order of 2 % of the mean value. Thus, if the change in Δ is of the same order of magnitude as the change in $\mu_0 H_c$ or $I_{50\%}^{100\,ns}$, it will not be detectable by this method.

Previously, strain induced changes of the PMA were observed in CoFeB thin films [124]. However, since the change of the anisotropy field H_K is on the order of a few percent, a change of Δ is not detected in our measurement.

7.6 Robust MTJ Performance under Strain

In conclusion, we have measured MTJ performance parameters under the application of mechanical strain. The strain was applied in a 4-point bending geometry, where the strain is constant over a large substrate area. It is found that the TMR ratio as well as the thermal

stability in the devices under test do not change as a function of strain within the measurement accuracy. The coercive field and the switching current decrease by approximately 2 % over the whole range of applied strain. A thinner free layer in our devices with PMA might contribute to the quantitative difference in the strain dependence of the TMR seen in previous work [71, 70]. The result reported here has significant implications for the manufacturability of STT-MRAM, as strain is often the result of device encapsulation or CMOS passivation processes that are determined by BEOL requirements.

Chapter 8

Conclusions and Outlook

Summary of this Thesis

A key challenge in the field of spin-orbit torque memory is the reduction of the critical switching current for a magnet with thermal stability Δ and thus improving the switching efficiency. In this thesis, we explored several approaches to address this challenge, including the use of ferrimagnets, topological insulators, and mechanical strain. In addition, experiments were presented to further the current physical understanding of spin-orbit torque switching and angular momentum transfer in magnetic hetero-structures. Here, we present a summary of the main results:

Angular Momentum Transfer in Ferrimagnets It is well understood that the anomalous Hall effect in transition metal/rare earth ferrimagnets depends only on the transition metal magnetization, because the conduction band in the transition metal is spin split. We reported that the switching sense in transition metal-rich and rare earth-rich samples is reversed with respect to the transition metal magnetization indicating that the spin-orbit torque angular momentum transfer follows the total magnetization of the ferrimagnet.

High Switching Efficiency in Ultra-Large Thickness GdFeCo We explored the thickness dependence of spin-orbit torque induced effective magnetic fields for the first time. We found that the effective fields scale inversely with thickness as expected from spin-torque theory. Further, we switched magnets with a thickness of up to 30 nm and showed high switching efficiencies compared to standard transition metal magnets, as shown in Fig 8.1.

Large Thermo-Electric Effects in Topological Insulators The spin-Hall angle is the ratio between the charge current and the generated spin current. It is often used as a metric for spin-torque efficiency. Recently, several research groups reported ultra-large spin-Hall angles in topological insulator films, even larger than unity. We were not able to reproduce these results. Instead, we measured large thermal voltages

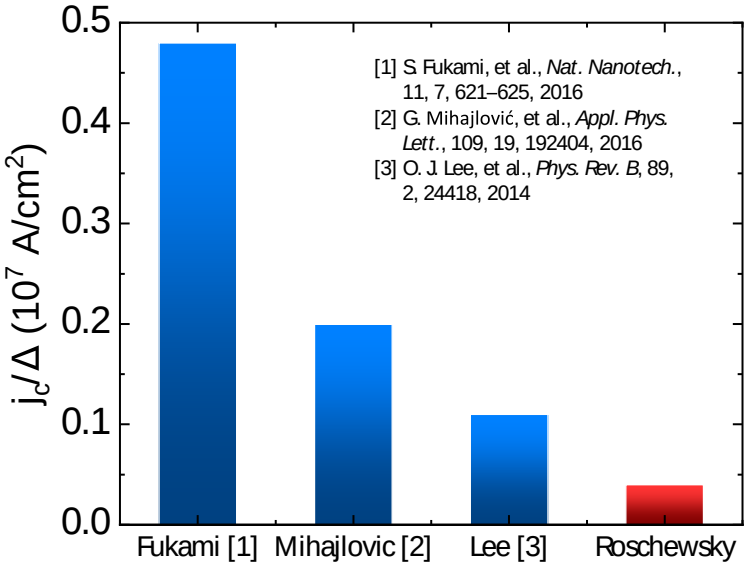

Figure 8.1: This graph compares the SOT switching efficiency j_c/Δ in our GdFeCo devices with other results in literature. A small value of j_c/Δ is desired for SOT memory applications.

stemming from the ordinary Nernst effect. These large thermal voltages may have led to an overestimation of the spin-Hall angle in previous experiments.

MTJ Robustness Under the Influence of Mechanical Strain The magnetic tunnel-junction performance under the influence of mechanical strain was discussed. We find that important performance parameters such as the critical switching current, the thermal stability, or the tunnel magneto-resistance do not depend significantly on the mechanical strain. This is in contrast to previous results on magnetic tunnel junctions with weak in-plane anisotropy.

Outlook and Future Work

While different approaches for the optimization of spin-orbit torque devices have been explored and evaluated in this thesis, spin-electronics is still a very active research field with many unexplored areas. Here, we highlight some open questions related to the work performed in this thesis for future research.

Spin Torque Switching in Terbium- or Dysprosium alloys In this thesis, we explored spin-orbit torque in ferrimagnetic GdFeCo and reported a high figure of merit for spin-orbit torque switching. To explore the role of the rare earth element for SOT switching further, it would be interesting to introduce additional rare earth elements, such as terbium or dysprosium, into the sample stack. This will modify the spin-orbit coupling,

the magnetic damping, and the perpendicular magnetic anisotropy of the magnet. Thus, Tb and Dy can impact spin-orbit torque switching significantly.

Spin Torque Switching in Ultra-Thick Ferrimagnets Switching experiments in ultra-thick GdFeCo alloys reported in this thesis were performed with relatively long current pulses with $\Delta t = 200\,\mu s$. An important task is to reduce the current pulse length and explore the switching dynamics of the ferrimagnetic alloy. Recently, a toggle-switching mechanism has been reported where GdFeCo alloys are switched with ultra-short heat pulses generated with the help of a femtosecond laser system. Combining the heat-driven toggle switching with spin-orbit coupling generated angular momentum transfer may pave a way for highly efficient and fast magnetization switching.

Scaling of GdFeCo Memory Devices We performed spin-orbit torque switching experiments with relatively large GdFeCo devices in the µm range. For memory applications, it will be important to explore the scaling of spin-torque switching as the lateral dimension of the GdFeCo device is reduced. This will require the used of advanced lithography techniques.

Tunnel Magneto-Resistance in GdFeCo Memory Devices Spin-orbit torque is an efficient technique to switch a ferromagnet. However, for the readout operation in magnetic memory, the tunnel magneto-resistance is usually employed. Thus, a future step will be to fabricate 3-terminal memory devices to explore spin-orbit torque switching and tunnel magneto-resistance readout in GdFeCo devices.

Spin-Torque Switching in Synthetic Ferrimagnets GdFeCo is an amorphous ferrimagnet with intrinsic ferrimagnetic ordering between the TM and RE sublattice. However, by stacking thin layers of Gd and FeCo, a synthetic ferrimagnet can be deposited. While many properties, such as the strong perpendicular anisotropy, can be observed in synthetic antiferromagnets as well, the antiferromagnetic coupling can be tuned more precisely by changing the thickness of the individual layers. Further, the interface to the heavy metal can be either the transition metal magnet or the rare earth magnet, allowing for additional tunability.

Spin-orbit torques in amorphous BiSe Harmonic measurement of the spin-orbit torque in epitaxial BiSb/Co samples revealed large thermal effects stemming from the ordinary Nernst effect. This is in contrast to measurements in sputtered BiSe reported by DC et al. [22], who reported an ultra-large spin-Hall angle ($\theta_{\mathrm{SH}} = 2ej_s/\hbar j_c = 1862\,\%$) but no sizable ordinary Nernst effect. Thus, harmonic Hall measurement should be performed in sputtered BiSe, with special care being given to the magnetic field dependence of the $V_{2\omega}$ signal to reveal the physical origin of the large voltage response.

Switching Efficiency in Topological Insulators While spin-orbit torque switching of topological insulator/ferromagnet heterostructures has been demonstrated by different groups, the figure of merit for spin torque switching in these devices has not been

reported. The topological insulator/ferromagnet interface can be rough and thus it is challenging to grow a ferromagnet with good thermal stability on top of a topological insulator. This makes a careful characterization of the thermal stability in such devices important.

Temperature Dependence of Spin-Orbit Torque The measurements reported in this thesis were performed at room temperature. However, based on previous reports, magneto-transport effects in topological insulators may be more pronounced at low temperatures. Thus, it would be interesting to repeat harmonic measurements reported in this thesis at low temperatures.

Compressive Strain in Tunnel Junctions It was shown that the performance of magnetic tunnel junctions with perpendicular magnetic anisotropy is robust to tensile strain. In addition, it is possible to explore tunnel junction performance with respect to compressive strain. The setup we designed can be modified to perform these types of measurements.

Epitaxial Strain in Tunnel Junctions The maximum strain that can be applied to the tunnel junctions in this report ($\epsilon \approx 0.06\,\%$) is limited by wafer breakage. However, through epitaxial growth methods, it may be possible to increase the strain applied to the magnet and the tunnel barrier. This increased strain could improve the MTJ performance.

The goal of this thesis was to further the understanding of spin-orbit torque driven angular momentum transfer and explore routes to improve the performance of magnetic memory devices. To this end, we explored spin-orbit torque in ferrimagnets and topological insulators and investigated MRAM performance under the application of mechanical strain. This thesis builds on the enormous progress that has been made in the field of magnetism within the last decade. We hope the results in this thesis will be useful for future technologies and encourage further research in the field of spintronics in the years to come.

Bibliography

[1] Tomoyoshi Aono. "The Nernst Effect of Bi-Sb Alloys". In: *Japanese Journal of Applied Physics* 9.7 (July 1970), pp. 761–767. ISSN: 0021-4922. DOI: 10.1143/JJAP.9.761. URL: http://stacks.iop.org/1347-4065/9/761.

[2] D Apalkov, B Dieny, and J M Slaughter. "Magnetoresistive Random Access Memory". In: *Proceedings of the IEEE* 104.10 (Oct. 2016), pp. 1796–1830. ISSN: 0018-9219. DOI: 10.1109/JPROC.2016.2590142. URL: http://dx.doi.org/10.1109/JPROC.2016.2590142.

[3] R Asomoza et al. "Extraordinary Hall effect in rareâĂŘearthâĂŞcobalt amorphous films". In: *J. Appl. Phys.* 48.9 (1977), p. 3829. URL: http://scitation.aip.org/content/aip/journal/jap/48/9/10.1063/1.324249.

[4] Can Onur Avci et al. "Interplay of spin-orbit torque and thermoelectric effects in ferromagnet/normal-metal bilayers". In: *Physical Review B* 90.22 (Dec. 2014), p. 224427. ISSN: 1098-0121. DOI: 10.1103/PhysRevB.90.224427. URL: https://link.aps.org/doi/10.1103/PhysRevB.90.224427.

[5] Can Onur Avci et al. "Origins of the Unidirectional Spin Hall Magnetoresistance in Metallic Bilayers". In: *Physical Review Letters* 121.8 (Aug. 2018), p. 087207. ISSN: 0031-9007. DOI: 10.1103/PhysRevLett.121.087207. URL: https://link.aps.org/doi/10.1103/PhysRevLett.121.087207.

[6] Can Onur Avci et al. "Unidirectional spin Hall magnetoresistance in ferromagnet/normal metal bilayers". In: *Nat Phys* 11.7 (July 2015), pp. 570–575. ISSN: 1745-2473. URL: http://dx.doi.org/10.1038/nphys3356.

[7] M. N. Baibich et al. "Giant Magnetoresistance of (001)Fe/(001)Cr Magnetic Superlattices". In: *Physical Review Letters* 61.21 (Nov. 1988), pp. 2472–2475. ISSN: 0031-9007. DOI: 10.1103/PhysRevLett.61.2472. URL: https://link.aps.org/doi/10.1103/PhysRevLett.61.2472.

[8] S A Baily and M B Salamon. "Berry-phase contribution to the anomalous Hall effect in gadolinium". In: *Phys. Rev. B* 71.10 (Mar. 2005), p. 104407. URL: http://link.aps.org/doi/10.1103/PhysRevB.71.104407.

[9] Lydia Baril et al. "Magnetostriction in spin valves". In: *Journal of Applied Physics* 85.8 (Apr. 1999), pp. 5139–5141. ISSN: 0021-8979. DOI: 10.1063/1.369103. URL: http://aip.scitation.org/doi/10.1063/1.369103.

[10] Kamran Behnia, Marie-Aude Méasson, and Yakov Kopelevich. "Nernst Effect in Semimetals: The Effective Mass and the Figure of Merit". In: *Physical Review Letters* 98.7 (Feb. 2007), p. 076603. ISSN: 0031-9007. DOI: 10.1103/PhysRevLett.98.076603. URL: https://link.aps.org/doi/10.1103/PhysRevLett.98.076603.

[11] L Berger. "Emission of spin waves by a magnetic multilayer traversed by a current". In: *Phys. Rev. B* 54 (Oct. 1996), pp. 9353–9358. DOI: 10.1103/PhysRevB.54.9353.

[12] L Berger. "Influence of spin-orbit interaction on the transport processes in ferromagnetic nickel alloys, in the presence of a degeneracy of the 3d band". In: *Physica* 30.6 (1964), pp. 1141–1159. ISSN: 0031-8914. URL: http://www.sciencedirect.com/science/article/pii/0031891464901053.

[13] Debanjan Bhowmik et al. "Deterministic Domain Wall Motion Orthogonal To Current Flow Due To Spin Orbit Torque". In: *Scientific Reports* 5 (July 2015), p. 11823. URL: http://dx.doi.org/10.1038/srep11823.

[14] Arne Brataas, Andrew D Kent, and Hideo Ohno. "Current-induced torques in magnetic materials". In: *Nat. Mater.* 11.5 (May 2012), pp. 372–381. ISSN: 1476-1122. URL: http://www.nature.com/nmat/journal/v11/n5/full/nmat3311.html.

[15] M S S Brooks, L Nordstrom, and B Johansson. "3d-5d band magnetism in rare earth-transition metal intermetallics: total and partial magnetic moments of the RFe 2 (R=Gd-Yb) Laves phase compounds". In: *J. Phys. Cond. Mat.* 3.14 (Apr. 1991), pp. 2357–2371. ISSN: 0953-8984. URL: http://stacks.iop.org/0953-8984/3/i=14/a=015.

[16] W. H. Butler et al. "Switching Distributions for Perpendicular Spin-Torque Devices Within the Macrospin Approximation". In: *IEEE Transactions on Magnetics* 48.12 (Dec. 2012), pp. 4684–4700. ISSN: 0018-9464. DOI: 10.1109/TMAG.2012.2209122. URL: http://ieeexplore.ieee.org/document/6242414/.

[17] Herbert B. Callen. "The Application of Onsager's Reciprocal Relations to Thermoelectric, Thermomagnetic, and Galvanomagnetic Effects". In: *Physical Review* 73.11 (June 1948), pp. 1349–1358. ISSN: 0031-899X. DOI: 10.1103/PhysRev.73.1349. URL: https://link.aps.org/doi/10.1103/PhysRev.73.1349.

[18] I A Campbell. "Indirect exchange for rare earths in metals". In: *J Phys F* 2.3 (1972), p. L47. URL: http://iopscience.iop.org/article/10.1088/0305-4608/2/3/004/.

[19] Jun-Yang Chen et al. "High Performance MgO-barrier Magnetic Tunnel Junctions for Flexible and Wearable Spintronic Applications". In: *Scientific Reports* 7 (Feb. 2017), p. 42001. ISSN: 2045-2322. DOI: 10.1038/srep42001. URL: http://www.nature.com/articles/srep42001.

[20] T. C. Chuang et al. "Enhancement of the anomalous Nernst effect in ferromagnetic thin films". In: *Physical Review B* 96.17 (Nov. 2017), p. 174406. ISSN: 2469-9950. DOI: 10.1103/PhysRevB.96.174406. URL: https://link.aps.org/doi/10.1103/PhysRevB.96.174406.

[21] Murat Cubukcu et al. "Ultra-Fast Perpendicular SpinâĂŞOrbit Torque MRAM". In: *IEEE Transactions on Magnetics* 54.4 (Apr. 2018), pp. 1–4. ISSN: 0018-9464. DOI: 10.1109/TMAG.2017.2772185. URL: http://ieeexplore.ieee.org/document/8291048/.

[22] Mahendra DC et al. "Room-temperature high spinâĂŞorbit torque due to quantum confinement in sputtered BixSe(1âĂŞx) films". In: *Nature Materials* 17.9 (Sept. 2018), pp. 800–807. ISSN: 1476-1122. DOI: 10.1038/s41563-018-0136-z. URL: http://www.nature.com/articles/s41563-018-0136-z.

[23] Praveen Deorani et al. "Observation of inverse spin Hall effect in bismuth selenide". In: *Physical Review B* 90.9 (Sept. 2014), p. 094403. ISSN: 1098-0121. DOI: 10.1103/PhysRevB.90.094403. URL: http://dx.doi.org/10.1103/PhysRevB.90.094403.

[24] Zhitao Diao et al. "Spin transfer switching and spin polarization in magnetic tunnel junctions with MgO and AlOx barriers". In: *Applied Physics Letters* 87.23 (Dec. 2005), p. 232502. ISSN: 0003-6951. DOI: 10.1063/1.2139849. URL: http://aip.scitation.org/doi/10.1063/1.2139849.

[25] M El-Hilo et al. "The sweep rate dependence of coercivity in recording media". In: *J. Mag. Mat.* 117 (1992), pp. L307 –L310. ISSN: 0304-8853. DOI: 10.1016/0304-8853(92)90085-3.

[26] Satoru Emori et al. "Current-driven dynamics of chiral ferromagnetic domain walls". In: *Nat. Mater.* 12.7 (July 2013), pp. 611–616. ISSN: 1476-1122. URL: http://www.nature.com/nmat/journal/v12/n7/abs/nmat3675.html.

[27] B N Engel et al. "A 4-Mb toggle MRAM based on a novel bit and switching method". In: *IEEE Trans. Mag.* 41 (2005), pp. 132–136. ISSN: 0018-9464. DOI: 10.1109/TMAG.2004.840847.

[28] Xin Fan et al. "Quantifying interface and bulk contributions to spinâĂŞorbit torque in magnetic bilayers". In: *Nat. Commun.* 5 (Jan. 2014), p. 3042. URL: http://www.nature.com/ncomms/2014/140109/ncomms4042/full/ncomms4042.html.

[29] Yabin Fan et al. "Magnetization switching through giant spinâĂŞorbit torque in a magnetically doped topological insulator heterostructure". In: *Nat. Mat.* 13.7 (Apr. 2014), pp. 699–704. ISSN: 1476-1122. DOI: 10.1038/nmat3973. URL: http://www.nature.com/doifinder/10.1038/nmat3973.

[30] Joseph Finley and Luqiao Liu. "Spin-Orbit-Torque Efficiency in Compensated Ferrimagnetic Cobalt-Terbium Alloys". In: *Phys. Rev. Applied* 6 (Nov. 2016), p. 54001. DOI: 10.1103/PhysRevApplied.6.054001.

[31] Kevin Garello et al. "Symmetry and magnitude of spin-orbit torques in ferromagnetic heterostructures". In: *Nat. Nano* 8.8 (Aug. 2013), pp. 587–593. ISSN: 1748-3387. URL: http://www.nature.com/nnano/journal/v8/n8/fullhtml.

[32] Kevin Garello et al. "Ultrafast magnetization switching by spin-orbit torques". In: *Appl. Ph.. L..* 105.21 (2014). ISSN: 00036951. DOI: 10.1063/1.4902443. eprint: 1310.5586. URL: http://aip.scitation.org/doi/abs/10.1063/1.4902443.

[33] P. Grünberg et al. "Layered Magnetic Structures: Evidence for Antiferromagnetic Coupling of Fe Layers across Cr Interlayers". In: *Physical Review Letters* 57.19 (Nov. 1986), pp. 2442–2445. ISSN: 0031-9007. DOI: 10.1103/PhysRevLett.57.2442. URL: https://link.aps.org/doi/10.1103/PhysRevLett.57.2442.

[34] Sachin Gupta et al. "Temperature dependence of ferromagnetic resonance spectra of permalloy on (Bi 1âĹŠ x Sb x) 2 Te 3". In: *Japanese Journal of Applied Physics* 57.2 (Feb. 2018), p. 020302. ISSN: 0021-4922. DOI: 10.7567/JJAP.57.020302. URL: http://stacks.iop.org/1347-4065/57/i=2/a=020302?key=crossref.0c82818d4ac30bc7c2d8d92f81d325a1.

[35] Woo Seung Ham et al. "Spin-orbit effective fields in Pt/GdFeCo bilayers". In: (Mar. 2017). arXiv: 1703.00995. URL: http://arxiv.org/abs/1703.00995.

[36] Jiahao Han et al. "Room-Temperature Spin-Orbit Torque Switching Induced by a Topological Insulator". In: *Physical Review Letters* 119.7 (Aug. 2017), p. 077702. ISSN: 0031-9007. DOI: 10.1103/PhysRevLett.119.077702. URL: https://link.aps.org/doi/10.1103/PhysRevLett.119.077702.

[37] Paul M Haney et al. "Current induced torques and interfacial spin-orbit coupling: Semiclassical modeling". In: *Phys. Rev. B* 87 (May 2013), p. 174411. DOI: 10.1103/PhysRevB.87.174411.

[38] Masamitsu Hayashi et al. "Quantitative characterization of the spin-orbit torque using harmonic Hall voltage measurements". In: *Phys. Rev. B* 89 (Apr. 2014), p. 144425. DOI: 10.1103/PhysRevB.89.144425.

[39] Pan He et al. "Bilinear magnetoelectric resistance as a probe of three-dimensional spin texture in topological surface states". In: *Nature Physics* 14 (Feb. 2018), p. 495. ISSN: 1745-2473. DOI: 10.1038/s41567-017-0039-y. URL: http://www.nature.com/articles/s41567-017-0039-y.

[40] F Hellman. "Measurement of magnetic anisotropy of ferrimagnets near compensation". In: *Appl. Phys. Lett.* 59.21 (1991). URL: http://aip.scitation.org/doi/abs/10.1063/1.105879.

[41] F. Hellman and E. M. Gyorgy. "Growth-induced magnetic anisotropy in amorphous Tb-Fe". In: *Physical Review Letters* 68.9 (Mar. 1992), pp. 1391–1394. ISSN: 0031-9007. DOI: 10.1103/PhysRevLett.68.1391. URL: https://link.aps.org/doi/10.1103/PhysRevLett.68.1391.

[42] Frances Hellman et al. "Interface-induced phenomena in magnetism". In: *Reviews of Modern Physics* 89.2 (June 2017), p. 025006. ISSN: 0034-6861. DOI: 10.1103/RevModPhys.89.025006. URL: http://link.aps.org/doi/10.1103/RevModPhys.89.025006.

[43] Kuo-Feng Huang et al. "Engineering spin-orbit torque in Co/Pt multilayers with perpendicular magnetic anisotropy". In: *Appl. Phys. Lett.* 107.23 (2015), p. 232407. URL: http://scitation.aip.org/content/aip/journal/apl/107/23/10.1063/1.4937443.

[44] T. Ideue et al. "Bulk rectification effect in a polar semiconductor". In: *Nature Physics* 13.6 (Mar. 2017), pp. 578–583. ISSN: 1745-2473. DOI: 10.1038/nphys4056. URL: http://www.nature.com/doifinder/10.1038/nphys4056.

[45] S Ikeda et al. "A perpendicular-anisotropy CoFeBâĂŞMgO magnetic tunnel junction". In: *Nat. Mat.* 9 (Sept. 2010), pp. 721–724. ISSN: 1476-1122. DOI: 10.1038/nmat2804.

[46] A. L. Jain. "Temperature Dependence of the Electrical Properties of Bismuth- Antimony Alloys". In: *Physical Review* 114.6 (June 1959), pp. 1518–1528. ISSN: 0031-899X. DOI: 10.1103/PhysRev.114.1518. URL: https://link.aps.org/doi/10.1103/PhysRev.114.1518.

[47] Mahdi Jamali et al. "Giant Spin Pumping and Inverse Spin Hall Effect in the Presence of Surface and Bulk SpinâĹŠOrbit Coupling of Topological Insulator Bi 2 Se 3". In: *Nano Letters* 15.10 (Oct. 2015), pp. 7126–7132. ISSN: 1530-6984. DOI: 10.1021/acs.nanolett.5b03274. URL: http://pubs.acs.org/doi/10.1021/acs.nanolett.5b03274.

[48] Xin Jiang et al. "Temperature Dependence of Current-Induced Magnetization Switching in Spin Valves with a Ferrimagnetic CoGd Free Layer". In: *Phys. Rev. Lett.* 97.21 (Nov. 2006), p. 217202. URL: http://link.aps.org/doi/10.1103/PhysRevLett.97.217202.

[49] Mark Johnson and R H Silsbee. "Interfacial charge-spin coupling: Injection and detection of spin magnetization in metals". In: *Phys. Rev. Lett.* 55.17 (Oct. 1985), pp. 1790–1793. URL: http://link.aps.org/doi/10.1103/PhysRevLett.55.1790.

[50] M. Julliere. "Tunneling between ferromagnetic films". In: *Physics Letters A* 54.3 (Sept. 1975), pp. 225–226. ISSN: 03759601. DOI: 10.1016/0375-9601(75)90174-7. URL: http://linkinghub.elsevier.com/retrieve/pii/0375960175901747.

[51] Seung H. Kang. "Embedded STT-MRAM for energy-efficient and cost-effective mobile systems". In: *2014 Symposium on VLSI Technology*. IEEE, June 2014, pp. 1–2. ISBN: 978-1-4799-3332-7. DOI: 10.1109/VLSIT.2014.6894354. URL: http://ieeexplore.ieee.org/lpdocs/epic03/wrapper.htm?arnumber=6894354.

[52] Robert Karplus and J M Luttinger. "Hall Effect in Ferromagnetics". In: *Phys. Rev.* 95.5 (Sept. 1954), pp. 1154–1160. URL: http://link.aps.org/doi/10.1103/PhysRev.95.1154.

[53] T. Kawahara et al. "Spin-transfer torque RAM technology: Review and prospect". In: *Microelectronics Reliability* 52.4 (Apr. 2012), pp. 613–627. ISSN: 00262714. DOI: 10.1016/j.microrel.2011.09.028. URL: http://linkinghub.elsevier.com/retrieve/pii/S002627141100446X.

[54] Nguyen Huynh Duy Khang, Yugo Ueda, and Pham Nam Hai. "A conductive topological insulator with large spin Hall effect for ultralow power spinâĂŞorbit torque switching". In: *Nature Materials* 17 (July 2018), 808âĂŞ813. ISSN: 1476-1122. DOI: 10.1038/s41563-018-0137-y. URL: http://www.nature.com/articles/s41563-018-0137-y.

[55] K. Kondou et al. "Fermi-level-dependent charge-to-spin current conversion by Dirac surface states of topological insulators". In: *Nature Physics* 12.11 (Nov. 2016), pp. 1027–1031. ISSN: 1745-2473. DOI: 10.1038/nphys3833. URL: http://www.nature.com/articles/nphys3833.

[56] Alexey A Kovalev, Arne Brataas, and Gerrit E W Bauer. "Spin transfer in diffusive ferromagnet/normal metal systems with spin-flip scattering". In: *Phys. Rev. B* 66.22 (Dec. 2002), p. 224424. URL: http://link.aps.org/doi/10.1103/PhysRevB.66.224424.

[57] Hwang-Rae Lee et al. "Spin-orbit torque in a bulk perpendicular magnetic anisotropy Pd/FePd/MgO system". In: *Sci. Rep.* 4 (Oct. 2014), p. 6548. URL: http://www.nature.com/articles/srep06548.

[58] Joon Sue Lee et al. "Mapping the chemical potential dependence of current-induced spin polarization in a topological insulator". In: *Physical Review B* 92.15 (Oct. 2015), p. 155312. ISSN: 1098-0121. DOI: 10.1103/PhysRevB.92.155312. URL: https://link.aps.org/doi/10.1103/PhysRevB.92.155312.

[59] Ki Seung Lee et al. "Threshold current for switching of a perpendicular magnetic layer induced by spin Hall effect". In: *Appl. Phys. Lett.* 102 (2013), p. 112410. DOI: 10.1063/1.4798288.

[60] O J Lee et al. "Central role of domain wall depinning for perpendicular magnetization switching driven by spin torque from the spin Hall effect". In: *Phys. Rev. B* 89.2 (Jan. 2014), p. 24418. DOI: 10.1103/PhysRevB.89.024418. URL: http://link.aps.org/doi/10.1103/PhysRevB.89.024418.

[61] S W Lee and K J Lee. "Emerging Three-Terminal Magnetic Memory Devices". In: *Proc. IEEE* 104 (Oct. 2016), pp. 1831–1843. ISSN: 0018-9219. DOI: 10.1109/JPROC.2016.2543782.

[62] B. Lenoir et al. "Transport properties of Bi-RICH Bi-Sb alloys". In: *Journal of Physics and Chemistry of Solids* 57.1 (Jan. 1996), pp. 89–99. ISSN: 00223697. DOI: 10.1016/0022-3697(95)00148-4. URL: http://linkinghub.elsevier.com/retrieve/pii/0022369795001484.

[63] Peng Li et al. "Spin-momentum locking and spin-orbit torques in magnetic nano-heterojunctions composed of Weyl semimetal WTe2". In: *Nature Communications* 9.1 (Dec. 2018), p. 3990. ISSN: 2041-1723. DOI: 10.1038/s41467-018-06518-1. URL: http://www.nature.com/articles/s41467-018-06518-1.

[64] Sheng San Li and T.A. Rabson. "The Nernst and the Seebeck effects in Te-doped BiSb alloys". In: *Solid-State Electronics* 13.2 (Feb. 1970), pp. 153–160. ISSN: 00381101. DOI: 10.1016/0038-1101(70)90045-6. URL: http://linkinghub.elsevier.com/retrieve/pii/0038110170900456.

[65] Luqiao Liu et al. "Current-Induced Switching of Perpendicularly Magnetized Magnetic Layers Using Spin Torque from the Spin Hall Effect". In: *Phys. Rev. Lett.* 109 (Aug. 2012), p. 96602. DOI: 10.1103/PhysRevLett.109.096602.

[66] Luqiao Liu et al. "Spin-polarized tunneling study of spin-momentum locking in topological insulators". In: *Physical Review B* 91.23 (June 2015), p. 235437. ISSN: 1098-0121. DOI: 10.1103/PhysRevB.91.235437. URL: https://link.aps.org/doi/10.1103/PhysRevB.91.235437.

[67] Luqiao Liu et al. "Spin-Torque Switching with the Giant Spin Hall Effect of Tantalum". In: *Science* 336 (2012), pp. 555–558. DOI: 10.1126/science.1218197.

[68] R. Lo Conte et al. "Spin-orbit torque-driven magnetization switching and thermal effects studied in Ta\CoFeB\MgO nanowires". In: *Appl. Phys. Lett.* 105.12 (Sept. 2014), p. 122404. ISSN: 0003-6951. DOI: 10.1063/1.4896225. URL: http://aip.scitation.org/doi/10.1063/1.4896225.

[69] M. Löhndorf et al. "Highly sensitive strain sensors based on magnetic tunneling junctions". In: *Applied Physics Letters* 81.2 (July 2002), pp. 313–315. ISSN: 0003-6951. DOI: 10.1063/1.1483123. URL: http://aip.scitation.org/doi/10.1063/1.1483123.

[70] Li Ming Loong et al. "Flexible MgO Barrier Magnetic Tunnel Junctions". In: *Advanced Materials* 28.25 (July 2016), pp. 4983–4990. ISSN: 09359648. DOI: 10.1002/adma.201600062. URL: http://doi.wiley.com/10.1002/adma.201600062.

[71] Li Ming Loong et al. "Strain-enhanced tunneling magnetoresistance in MgO magnetic tunnel junctions". In: *Scientific Reports* 4.1 (May 2015), p. 6505. ISSN: 2045-2322. DOI: 10.1038/srep06505. URL: http://www.nature.com/articles/srep06505.

[72] Yang Lv et al. "Unidirectional spin-Hall and RashbaâĹŠEdelstein magnetoresistance in topological insulator-ferromagnet layer heterostructures". In: *Nature Communications* 9.1 (Jan. 2018), p. 111. ISSN: 2041-1723. DOI: 10.1038/s41467-017-02491-3. URL: http://www.nature.com/articles/s41467-017-02491-3.

[73] R Malmhäll. "Extraordinary Hall resistivity in amorphous terbiumâĂŞiron thin films and its temperature dependence". In: *J. Appl. Phys.* 54.9 (1983), p. 5128. URL: http://scitation.aip.org/content/aip/journal/jap/54/9/10.1063/1.332735.

[74] A. R. Mellnik et al. "Spin-transfer torque generated by a topological insulator". In: *Nature* 511.7510 (July 2014), pp. 449–451. ISSN: 0028-0836. DOI: 10.1038/nature13534. URL: http://www.nature.com/doifinder/10.1038/nature13534.

[75] J. B. S. Mendes et al. "Dirac-surface-state-dominated spin to charge current conversion in the topological insulator $Bi_{0.22}Sb_{0.78}$". In: *Physical Review B* 96.18 (Nov. 2017), p. 180415. ISSN: 2469-9950. DOI: 10.1103/PhysRevB.96.180415. URL: https://link.aps.org/doi/10.1103/PhysRevB.96.180415.

[76] D. Meyners et al. "Pressure sensor based on magnetic tunnel junctions". In: *Journal of Applied Physics* 105.7 (Apr. 2009), p. 07C914. ISSN: 0021-8979. DOI: 10.1063/1.3063662. URL: http://aip.scitation.org/doi/10.1063/1.3063662.

[77] Ioan Mihai Miron et al. "Current-driven spin torque induced by the Rashba effect in a ferromagnetic metal layer". In: *Nat. Mater.* 9.3 (Mar. 2010), pp. 230–234. ISSN: 1476-1122. URL: http://www.nature.com/nmat/journal/v9/n3/abs/nmat2613.html.

[78] Y Mimura, N Imamura, and Y Kushiro. "Hall effect in rare earthâĂŞtransition metal amorphous alloy films". In: *J. Appl. Phys.* 47.7 (1976), p. 5128. URL: http://scitation.aip.org/content/aip/journal/jap/47/7/10.1063/1.323098.

[79] Ioan Mihai Miron et al. "Perpendicular switching of a single ferromagnetic layer induced by in-plane current injection". In: *Nature* 476.7359 (Aug. 2011), pp. 189–193. ISSN: 0028-0836. URL: http://www.nature.com/nature/journal/v476/n7359/abs/nature10309.html.

[80] Rahul Mishra et al. "Anomalous current-induced spin torques in ferrimagnets near compensation". In: (Mar. 2017). arXiv: 1703.08263. URL: http://arxiv.org/abs/1703.08263.

[81] J. S. Moodera et al. "Large Magnetoresistance at Room Temperature in Ferromagnetic Thin Film Tunnel Junctions". In: *Physical Review Letters* 74.16 (Apr. 1995), pp. 3273–3276. ISSN: 0031-9007. DOI: 10.1103/PhysRevLett.74.3273. URL: https://link.aps.org/doi/10.1103/PhysRevLett.74.3273.

[82] Naoto Nagaosa et al. "Anomalous Hall effect". In: *Rev. Mod. Phys.* 82.2 (May 2010), pp. 1539–1592. URL: http://link.aps.org/doi/10.1103/RevModPhys.82.1539.

[83] P. Noel et al. "Highly Efficient Spin-to-Charge Current Conversion in Strained HgTe Surface States Protected by a HgCdTe Layer". In: *Physical Review Letters* 120.16 (Apr. 2018), p. 167201. ISSN: 0031-9007. DOI: 10.1103/PhysRevLett.120.167201. URL: https://link.aps.org/doi/10.1103/PhysRevLett.120.167201.

[84] J J Nowak et al. "Demonstration of Ultralow Bit Error Rates for Spin-Torque Magnetic Random-Access Memory With Perpendicular Magnetic Anisotropy". In: *IEEE Magnetics Letters* 2 (2011), pp. 3000204–3000204. ISSN: 1949-307X. DOI: 10.1109/LMAG.2011.2155625. URL: http://ieeexplore.ieee.org/document/5875962/.

[85] Masaru Onoda and Naoto Nagaosa. "Topological Nature of Anomalous Hall Effect in Ferromagnets". In: *J. Phys. Soc. Jap.* 71.1 (2002), pp. 19–22. URL: http://journals.jps.jp/doi/abs/10.1143/JPSJ.71.19.

[86] Shinya Ota, Akira Ando, and Daichi Chiba. "A flexible giant magnetoresistive device for sensing strain direction". In: *Nature Electronics* 1.2 (Feb. 2018), pp. 124–129. ISSN: 2520-1131. DOI: 10.1038/s41928-018-0022-3. URL: http://www.nature.com/articles/s41928-018-0022-3.

[87] Chi Feng Pai et al. "Determination of spin torque efficiencies in heterostructures with perpendicular magnetic anisotropy". In: *Phys. Rev. B* 93.14 (Apr. 2016), p. 144409. ISSN: 2469-9950. DOI: 10.1103/PhysRevB.93.144409. URL: https://link.aps.org/doi/10.1103/PhysRevB.93.144409.

[88] O Paul and H Baltes. "Thermal conductivity of CMOS materials for the optimization of microsensors". In: *Journal of Micromechanics and Microengineering* 3.3 (Sept. 1993), pp. 110–112. ISSN: 0960-1317. DOI: 10.1088/0960-1317/3/3/003. URL: www.doi.org/10.1088/0960-1317/3/3/003.

[89] A Pogorily, E Shypil, and C Alexander. "A study of magnetization in exchange-coupled FM/Gd bilayers". In: *J. Mag. Mater.* 286 (2005), pp. 493–496. ISSN: 0304-8853. URL: https://doi.org/10.1016/j.jmmm.2004.09.104.

[90] Xuepeng Qiu et al. "SpinâĂŞorbit-torque engineering via oxygen manipulation". In: *Nat. Nano.* 10.4 (May 2015), pp. 333–338. ISSN: 1748-3387. URL: http://www.nature.com/nnano/journal/v10/n4/abs/nnano.2015.18.html.

[91] J.-C. Rojas-Sánchez et al. "Spin Pumping and Inverse Spin Hall Effect in Platinum: The Essential Role of Spin-Memory Loss at Metallic Interfaces". In: *Physical Review Letters* 112.10 (Mar. 2014), p. 106602. ISSN: 0031-9007. DOI: 10.1103/PhysRevLett.112.106602. URL: https://link.aps.org/doi/10.1103/PhysRevLett.112.106602.

[92] J.-C. Rojas-Sánchez et al. "Spin to Charge Conversion at Room Temperature by Spin Pumping into a New Type of Topological Insulator: α-Sn Films". In: *Physical Review Letters* 116.9 (Mar. 2016), p. 096602. ISSN: 0031-9007. DOI: 10.1103/PhysRevLett.116.096602. URL: https://link.aps.org/doi/10.1103/PhysRevLett.116.096602.

[93] Niklas Roschewsky et al. "Perpendicular magnetic tunnel junction performance under mechanical strain". In: *Applied Physics Letters* 112.23 (June 2018), p. 232401. ISSN: 0003-6951. DOI: 10.1063/1.5034145. URL: http://aip.scitation.org/doi/10.1063/1.5034145.

[94] Niklas Roschewsky et al. "Spin-orbit torque and Nernst effect in Bi-Sb/Co heterostructures". In: *Physical Review B* 99.19 (May 2019), p. 195103. ISSN: 2469-9950. DOI: 10.1103/PhysRevB.99.195103. URL: https://link.aps.org/doi/10.1103/PhysRevB.99.195103.

[95] Niklas Roschewsky et al. "Spin-orbit torque switching of ultralarge-thickness ferrimagnetic GdFeCo". In: *Physical Review B* 96.6 (Aug. 2017), p. 064406. ISSN: 2469-9950. DOI: 10.1103/PhysRevB.96.064406. URL: http://link.aps.org/doi/10.1103/PhysRevB.96.064406.

[96] Niklas Roschewsky et al. "Spin-orbit torques in ferrimagnetic GdFeCo alloys". In: *Appl. Phys. Lett.* 109 (2016), p. 112403. DOI: 10.1063/1.4962812.

[97] Hideo Sato et al. "MgO/CoFeB/Ta/CoFeB/MgO Recording Structure in Magnetic Tunnel Junctions With Perpendicular Easy Axis". In: *IEEE Transactions on Magnetics* 49.7 (July 2013), pp. 4437–4440. ISSN: 0018-9464. DOI: 10.1109/TMAG.2013.2251326. URL: http://ieeexplore.ieee.org/document/6558971/.

[98] Michael Schreier et al. "Current heating induced spin Seebeck effect". In: *Applied Physics Letters* 103.24 (Dec. 2013), p. 242404. ISSN: 0003-6951. DOI: 10.1063/1.4839395. URL: http://aip.scitation.org/doi/10.1063/1.4839395.

[99] Shuyuan Shi et al. "Efficient charge-spin conversion and magnetization switching through the Rashba effect at topological-insulator/Ag interfaces". In: *Physical Review B* 97.4 (Jan. 2018), p. 041115. ISSN: 2469-9950. DOI: 10.1103/PhysRevB.97.041115. URL: https://link.aps.org/doi/10.1103/PhysRevB.97.041115.

[100] Y. Shiomi et al. "Spin-Electricity Conversion Induced by Spin Injection into Topological Insulators". In: *Physical Review Letters* 113.19 (Nov. 2014), p. 196601. ISSN: 0031-9007. DOI: 10.1103/PhysRevLett.113.196601. URL: https://link.aps.org/doi/10.1103/PhysRevLett.113.196601.

[101] T Shirakawa et al. "The Kerr and the Hall Effects in Amorphous Magnetic Films". In: *AIP Conf. Proc.* 34.1 (1976), p. 349. URL: http://scitation.aip.org/content/aip/proceeding/aipcp/10.1063/1.2946125.

[102] D. Shum et al. "CMOS-embedded STT-MRAM arrays in 2x nm nodes for GP-MCU applications". In: *2017 Symposium on VLSI Technology*. IEEE, June 2017, T208–T209. ISBN: 978-4-86348-605-8. DOI: 10.23919/VLSIT.2017.7998174. URL: http://ieeexplore.ieee.org/document/7998174/.

[103] J C Slonczewski. "Current-driven excitation of magnetic multilayers". In: *J. Mag. Mat.* 159 (1996), pp. L1 –L7. ISSN: 0304-8853. DOI: 10.1016/0304-8853(96)00062-5.

[104] J Smit. "The spontaneous hall effect in ferromagnetics I". In: *Physica* 21.6 (1955), pp. 877–887. ISSN: 0031-8914. URL: http://www.sciencedirect.com/science/article/pii/S0031891455925969.

[105] Y. J. Song et al. "Highly functional and reliable 8Mb STT-MRAM embedded in 28nm logic". In: *2016 IEEE International Electron Devices Meeting*. IEEE, Dec. 2016, pp. 27.2.1–27.2.4. ISBN: 978-1-5090-3902-9. DOI: 10.1109/IEDM.2016.7838491. URL: http://ieeexplore.ieee.org/document/7838491/.

[106] C D Stanciu et al. "Ultrafast spin dynamics across compensation points in ferrimagnetic \mathrm{GdFeCo}: The role of angular momentum compensation". In: *Phys. Rev. B* 73.22 (June 2006), p. 220402. URL: http://link.aps.org/doi/10.1103/PhysRevB.73.220402.

[107] J. Z. Sun. "Spin-current interaction with a monodomain magnetic body: A model study". In: *Physical Review B* 62.1 (July 2000), pp. 570–578. ISSN: 0163-1829. DOI: 10.1103/PhysRevB.62.570. URL: https://link.aps.org/doi/10.1103/PhysRevB.62.570.

[108] Ali Tavassolizadeh et al. "Highly strain-sensitive magnetostrictive tunnel magnetoresistance junctions". In: *Journal of Magnetism and Magnetic Materials* 384 (June 2015), pp. 308–313. ISSN: 03048853. DOI: 10.1016/j.jmmm.2015.01.083. URL: http://linkinghub.elsevier.com/retrieve/pii/S0304885315001262.

[109] Ali Tavassolizadeh et al. "Tunnel Magnetoresistance Sensors with Magnetostrictive Electrodes: Strain Sensors". In: *Sensors* 16.11 (Nov. 2016), p. 1902. ISSN: 1424-8220. DOI: 10.3390/s16111902. URL: http://www.mdpi.com/1424-8220/16/11/1902.

[110] Yoshihiro Terada et al. "Thermal conductivity of cobalt-base alloys". In: *Metallurgical and Materials Transactions A* 34.9 (Sept. 2003), pp. 2026–2028. ISSN: 1073-5623. DOI: 10.1007/s11661-003-0168-z. URL: http://link.springer.com/10.1007/s11661-003-0168-z.

[111] Kohei Ueda et al. "Effect of rare earth metal on the spin-orbit torque in magnetic heterostructures". In: *Appl. Phys. Lett.* 108.23 (June 2016), p. 232405. ISSN: 0003-6951. DOI: 10.1063/1.4953348. URL: http://aip.scitation.org/doi/10.1063/1.4953348.

[112] Kohei Ueda et al. "Spin-orbit torques in Ta/TbxCo100-x ferrimagnetic alloy films with bulk perpendicular magnetic anisotropy". In: *Appl. Phys. Lett.* 109 (2016), p. 232403. DOI: 10.1063/1.4971393.

[113] Yugo Ueda et al. "Epitaxial growth and characterization of Bi1-xSbx spin Hall thin films on GaAs(111)A substrates". In: *Applied Physics Letters* 110.6 (Feb. 2017), p. 062401. ISSN: 0003-6951. DOI: 10.1063/1.4975492. URL: http://aip.scitation.org/doi/10.1063/1.4975492.

[114] Hailong Wang et al. "Surface-State-Dominated Spin-Charge Current Conversion in Topological-InsulatorâĂŞFerromagnetic-Insulator Heterostructures". In: *Physical Review Letters* 117.7 (Aug. 2016), p. 076601. ISSN: 0031-9007. DOI: 10.1103/PhysRevLett.117.076601. URL: https://link.aps.org/doi/10.1103/PhysRevLett.117.076601.

[115] P. Wang et al. "Unidirectional Spin-Wave-Propagation-Induced Seebeck Voltage in a PEDOT:PSS/YIG Bilayer". In: *Physical Review Letters* 120.4 (Jan. 2018), p. 047201. ISSN: 0031-9007. DOI: 10.1103/PhysRevLett.120.047201. URL: https://link.aps.org/doi/10.1103/PhysRevLett.120.047201.

[116] Yi Wang et al. "Room temperature magnetization switching in topological insulator-ferromagnet heterostructures by spin-orbit torques". In: *Nature Communications* 8.1 (Dec. 2017), p. 1364. ISSN: 2041-1723. DOI: 10.1038/s41467-017-01583-4. URL: http://www.nature.com/articles/s41467-017-01583-4.

[117] Yi Wang et al. "Topological Surface States Originated Spin-Orbit Torques in Bi2Se3". In: *Physical Review Letters* 114.25 (June 2015), p. 257202. ISSN: 0031-9007. DOI: 10.1103/PhysRevLett.114.257202. URL: https://link.aps.org/doi/10.1103/PhysRevLett.114.257202.

[118] Seonghoon Woo et al. "Enhanced spin-orbit torques in Pt/Co/Ta heterostructures". In: *Appl. Phys. Lett.* 105 (2014), p. 212404. DOI: 10.1063/1.4902529.

[119] D. C. Worledge et al. "Spin torque switching of perpendicular TaâĹčCoFeBâĹčMgO-based magnetic tunnel junctions". In: *Applied Physics Letters* 98.2 (Jan. 2011), p. 022501. ISSN: 0003-6951. DOI: 10.1063/1.3536482. URL: http://aip.scitation.org/doi/10.1063/1.3536482.

[120] H X Yang et al. "First-principles investigation of the very large perpendicular magnetic anisotropy at Fe$|$MgO and Co$|$MgO interfaces". In: *Phys. Rev. B* 84 (Aug. 2011), p. 54401. DOI: 10.1103/PhysRevB.84.054401.

[121] K. Yasuda et al. "Current-Nonlinear Hall Effect and Spin-Orbit Torque Magnetization Switching in a Magnetic Topological Insulator". In: *Physical Review Letters* 119.13 (Sept. 2017), p. 137204. ISSN: 0031-9007. DOI: 10.1103/PhysRevLett.119.137204. URL: https://link.aps.org/doi/10.1103/PhysRevLett.119.137204.

[122] K. Yasuda et al. "Large Unidirectional Magnetoresistance in a Magnetic Topological Insulator". In: *Physical Review Letters* 117.12 (Sept. 2016), p. 127202. ISSN: 0031-9007. DOI: 10.1103/PhysRevLett.117.127202. URL: https://link.aps.org/doi/10.1103/PhysRevLett.117.127202.

[123] T. Yazaki. "Thermal Conductivity of Bismuth-Antimony Alloy Single Crystals". In: *Journal of the Physical Society of Japan* 25.4 (Oct. 1968), pp. 1054–1060. ISSN: 0031-9015. DOI: 10.1143/JPSJ.25.1054. URL: http://journals.jps.jp/doi/10.1143/JPSJ.25.1054.

[124] Guoqiang Yu et al. "Strain-induced modulation of perpendicular magnetic anisotropy in Ta/CoFeB/MgO structures investigated by ferromagnetic resonance". In: *Applied Physics Letters* 106.7 (Feb. 2015), p. 072402. ISSN: 0003-6951. DOI: 10.1063/1.4907677. URL: http://aip.scitation.org/doi/10.1063/1.4907677.

[125] Di Yue et al. "Spin-to-Charge Conversion in Bi Films and Bi/Ag Bilayers". In: *Physical Review Letters* 121.3 (July 2018), p. 037201. ISSN: 0031-9007. DOI: 10.1103/PhysRevLett.121.037201. URL: https://link.aps.org/doi/10.1103/PhysRevLett.121.037201.

[126] Zhengyang Zhao et al. "Spin Hall switching of the magnetization in Ta/TbFeCo structures with bulk perpendicular anisotropy". In: *Appl. Phys. Lett.* 106 (2015), p. 132404. DOI: 10.1063/1.4916665.